

# A Simulation Framework for Optimizing High-Fidelity, QND Readout of Transmon Qubits via Qubit-Resonator Detuning

Alexander Osherov

Thesis for the attainment of the academic degree

**Bachelor of Science**

at the TUM School of Natural Sciences of the Technical University of Munich

**Supervisor:**

Prof. Dr. Stefan Filipp

**Advisors:**

J. Englhardt  
Dr. B. Lienhard

**Submitted:**

Munich, 7. October 2025



I hereby declare that this thesis is entirely the result of my own work except where otherwise indicated. I have only used the resources given in the list of references.



## Abstract

Qubit-state readout is essential to quantum computing. Superconducting qubits, out of which the transmon is the most prominent, are generally read out in the dispersive regime. This regime enables the measured qubit state to be preserved, referred to as a quantum non-demolition (QND) measurement. We are interested in fast measurements, thus we are using high-power readout pulses, which can be plagued by undesired measurement-induced state transitions (MISTs). They are characterized by a change in the qubit state during the measurement, compromising the QNDness of the readout.

To investigate the trade-off between readout speed, fidelity, and QND behaviour, we employ two complementary simulation frameworks. The first one, based on the work of Wong et al. [Won+23], models the entire measurement chain to predict the readout fidelity. It works by calculating the output signal to a readout pulse based on the system's  $S_{21}$ -parameters and then adding realistic noise contributions from the cryogenic amplification path. The second framework, developed by Dumas et al. [Dum+24], uses semiclassical Floquet analysis to calculate the critical photon number in the resonator. They identify an upper limit for the readout power where the measurements remain QND.

In this thesis, we combine these frameworks to study different qubit-resonator detunings and determine a parameter regime that minimizes measurement-induced transitions while preserving high readout fidelity.

## Zusammenfassung

Die Auslesung von Qubit-Zuständen ist für das Quantencomputing unerlässlich. Supraleitende Qubits, unter denen das Transmon am prominentesten ist, werden im Allgemeinen im dispersiven Regime ausgelesen. Dieses Regime ermöglicht es, den gemessenen Qubit-Zustand zu erhalten, was als quantenzerstörungsfreie (QND) Messung bezeichnet wird. Da wir an schnellen Messungen interessiert sind, verwenden wir Auslesepulse mit hoher Leistung, die jedoch durch unerwünschte messinduzierte Zustandsübergänge (MISTs) beeinträchtigt werden können. Diese sind durch eine Änderung des Qubit-Zustands während der Messung gekennzeichnet, was das QND-Prinzip der Auslesung verletzt.

Um den Zielkonflikt zwischen Auslesegeschwindigkeit, Fidelität und QND-Verhalten zu untersuchen, verwenden wir zwei komplementäre Simulations-Frameworks. Das erste, basierend auf der Arbeit von Wong et al. [Won+23], modelliert die gesamte Messkette, um die Auslesefidelität vorherzusagen. Dabei wird das Ausgangssignal eines Auslesepulses auf der Grundlage der  $S_{21}$ -Parameter des Systems berechnet und anschließend werden realistische Rauschbeiträge aus dem kryogenen Verstärkerpfad hinzugefügt. Das zweite Framework, entwickelt von Dumas et al. [Dum+24], nutzt eine semiklassische Floquet-Analyse, um die kritische Photonenzahl im Resonator zu berechnen. Damit wird eine Obergrenze für die Ausleseleistung identifiziert, bei der die Messungen QND-Verhalten aufweisen.

In dieser Arbeit kombinieren wir diese Frameworks, um verschiedene Qubit-Resonator-Verstimmungen zu untersuchen und einen Parameterbereich zu bestimmen, der messinduzierte Übergänge minimiert und gleichzeitig eine hohe Auslesefidelität gewährleistet.



# Contents

<b>1</b>	<b>Introduction</b>	<b>1</b>
<b>2</b>	<b>Theoretical Background</b>	<b>3</b>
2.1	Transmon Qubits . . . . .	3
2.1.1	From a Simple LC Circuit to a Qubit . . . . .	3
2.1.2	Dealing with Charge Noise . . . . .	4
2.2	The Jaynes-Cummings Model and Dispersive Coupling . . . . .	4
2.3	Qubit Readout . . . . .	6
	Dispersive Readout Principle . . . . .	6
	Heterodyne Detection and Demodulation . . . . .	6
2.3.1	S-Parameters . . . . .	8
2.4	Measurement-Induced State Transitions (MISTs) . . . . .	8
2.4.1	Semiclassical Analysis . . . . .	9
	Floquet's Theorem and Quasienergies . . . . .	10
2.5	Relating Input Power to Photon Number . . . . .	11
<b>3</b>	<b>Methodology</b>	<b>13</b>
3.1	Fidelity Simulation Framework . . . . .	13
3.1.1	Core Methodology . . . . .	13
	Noise Modeling . . . . .	14
3.1.2	Our Implementation and Key Additions . . . . .	14
	S-Parameters . . . . .	14
	IQ Projection . . . . .	15
	Comparison to existing Simulation . . . . .	15
3.1.3	Analysis of Readout Fidelity versus Qubit-Resonator Detuning . . . . .	15
	Large Detuning ( $> 4$ GHz) . . . . .	16
	Optimal Detuning (from 3.2 to 1.8 GHz) . . . . .	16
	Small Detuning ( $< 1.5$ GHz) . . . . .	17
3.2	MIST Prediction Framework . . . . .	17
<b>4</b>	<b>Results and Discussion</b>	<b>21</b>
4.1	Constrained Fidelity Analysis . . . . .	21
4.1.1	Interpretation of Results . . . . .	22
	Small Detuning Regime . . . . .	22
	Large Detuning Regime . . . . .	22
	Optimal Operating Window . . . . .	22
<b>5</b>	<b>Conclusion and Outlook</b>	<b>25</b>
<b>Appendix</b>		<b>27</b>
A	Additional Figures . . . . .	27
B	Tables . . . . .	28
<b>Bibliography</b>		<b>31</b>



# 1 Introduction

High-fidelity, qubit state readout, maintaining the measurement state, is an important requirement for efficient quantum computing. The latter property defines a quantum non-demolition (QND) measurement [Bla+04]. In superconducting architectures, this is usually achieved through a dispersive readout scheme in a circuit QED (cQED) setup [Bla+21], which involves probing an off-resonantly coupled resonator with a microwave pulse.

Dispersive readout comprises a critical trade-off between the measurement speed and fidelity. To make qubit-state readout faster, we use shorter measurement pulses. However, a shorter pulse duration reduces the information content [Bla+21], thereby lowering fidelity. While increasing the probe power can compensate for this loss [Won+23], it also increases the probability of exciting the qubit into higher non-computational energy levels—an error known as a measurement-induced state transition (MIST), or "qubit ionization" [Dum+24]. This phenomenon compromises the QNDness of the measurement and poses a significant problem in the development of fault-tolerant quantum computers. This thesis confronts this challenge by investigating alternative qubit-resonator detuning regimes for a transmon qubit, with the goal of enabling fast, high-fidelity readouts that reduce transmon ionization.

To achieve this, we developed and combined two distinct numerical simulations. The first, following the work of Wong et al. [Won+23], is a fidelity simulation designed to predict readout accuracy as a function of key system and pulse parameters. This model will quantify the relationship between fidelity and variables such as the duration and power of the readout pulse, detuning, and environmental noise.

The second simulation implements the semiclassical model described by Dumas et al. [Dum+24] to determine the critical photon number in the resonator above which state transitions are likely to occur. By treating the resonator field as a classical drive on the transmon, this computationally efficient model accurately predicts the onset of qubit ionization.

Finally, these two simulations are integrated to perform a comprehensive analysis. The critical photon number derived from the second simulation serves as a constraint on the maximum readout power in the first simulation. This combined methodology enables a systematic study of how readout fidelity varies with detuning for pulses that remain safely below the ionization threshold. The ultimate aim is to provide a robust framework for optimizing the design of cQED setups [Bla+21] and readout pulses to achieve a truly high-fidelity and QND readout for transmon qubits.



## 2 Theoretical Background

The foundational concepts and theoretical descriptions presented in this chapter for the transmon qubit (Section 2.1), the Jaynes-Cummings model (Section 2.2), and qubit readout (Section 2.3) are primarily based on the comprehensive review articles [Kra+19] and [Bla+21].

### 2.1 Transmon Qubits

A quantum bit, or qubit, is a quantum mechanical two-level system. To function as a qubit, this system must have distinguishable energy levels that can be selectively manipulated to function as a qubit.

#### 2.1.1 From a Simple LC Circuit to a Qubit

A simple LC resonant circuit has a Hamiltonian,  $H$ , given by:

$$\hat{H} = 4E_C\hat{n}^2 + \frac{1}{2}E_L\hat{\phi}^2, \quad (2.1)$$

where  $L$  and  $C$  are the inductance and capacitance of the circuit, respectively,  $E_C = e^2/(2C)$  is the charging energy with  $e$  as the elementary charge,  $\hat{n}$  is the number operator of Cooper pairs on the capacitor island,  $E_L = (\hbar/2e)^2/L$  (with  $\hbar$  the reduced Planck constant) is the inductive energy, and  $\hat{\phi}$  is the superconducting phase difference across the inductor.

In this circuit, the energy levels are all equally spaced, as shown for a quantum harmonic oscillator in Figure 2.1(a,b).

By replacing the linear inductor with a Josephson junction, we obtain an anharmonic potential [Figure 2.1(c,d)], which results in non-equidistant energy levels and enables selective addressing of the qubit states. The Hamiltonian then changes to:

$$\hat{H} = 4E_C(\hat{n} - n_g)^2 - E_J \cos(\hat{\phi}), \quad (2.2)$$

where  $E_J = \hbar I_c/(2e)$  is the Josephson energy (with  $I_c$  the junction's critical current, and  $e$  the elementary charge), and  $\hat{\phi}$  is the superconducting phase difference across the Josephson junction. The offset charge  $n_g$  is explained later in Section 2.1.2.

The anharmonicity is given by  $\alpha = \omega_{12} - \omega_{01} \neq 0$ , where  $\omega_{01}$  and  $\omega_{12}$  are the transition frequencies between the energy levels. This allows for selective addressing of the computational states  $|0\rangle$  and  $|1\rangle$ .

While it is treated as a two-level system for most operations, the existence of higher energy levels must be considered in some cases, for example, when discussing Measurement-Induced State Transitions (Section 2.4).

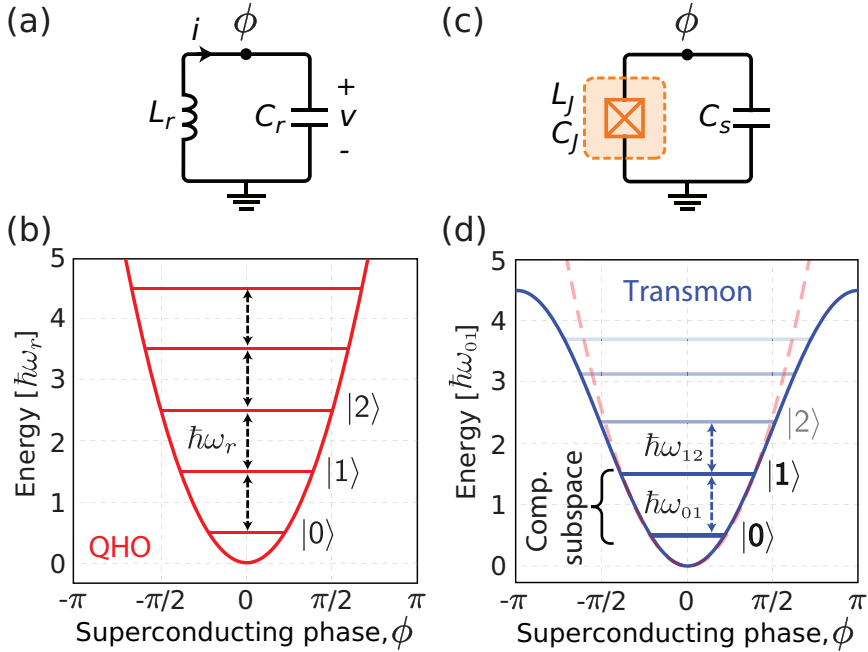


**Figure 2.1** Potential energy landscape and energy levels of a quantum harmonic oscillator (QHO) compared to a transmon qubit. The QHO (a) has equally spaced energy levels (b), while the transmon’s (c) anharmonic potential (d) leads to non-equidistant levels, enabling selective control of qubit states. Figure taken from [Kra+19].

### 2.1.2 Dealing with Charge Noise

The additional term,  $n_g$ , that appears in the transmon Hamiltonian Equation (2.2) represents an unwanted background electric charge that can fluctuate, causing what is known as charge noise. In initial superconducting qubit designs, this noise made the system very unstable.

The transmon qubit solves this problem by design. It is operated in a specific regime where the ratio of the Josephson energy ( $E_J$ ) to the charging energy ( $E_C$ ) is very large:

$$\frac{E_J}{E_C} \gg 1. \quad (2.3)$$

In this state, the qubit’s energy levels are exponentially insensitive to the charge noise. This makes the qubit much more stable and helps it maintain its quantum state for a longer time, a property known as coherence. While the anharmonicity is also reduced in this regime, its reduction scales more favorably as a weak power law. This trade-off between charge noise immunity and anharmonicity is what makes the transmon a workable qubit design.

## 2.2 The Jaynes-Cummings Model and Dispersive Coupling

The interaction between a superconducting qubit, such as the transmon discussed in Section 2.1, and the readout resonator is described by the Jaynes-Cummings (JC) model. This model, which describes the coupling between a two-level system and a single mode of a quantized electromagnetic field, provides the theoretical foundation for modern superconducting qubit readout schemes.

The Hamiltonian for the JC model is given by:

$$H_{\text{JC}} = \hbar\omega_r a^\dagger a + \frac{\hbar\omega_q}{2} \sigma_z + \hbar g(a^\dagger \sigma^- + a \sigma^+). \quad (2.4)$$

Here, the first term describes the free Hamiltonian of the readout resonator with frequency  $\omega_r$ , where  $a^\dagger$  and  $a$  are the creation and annihilation operators, respectively. The second term describes the qubit with the transition frequency  $\omega_q$ , with  $\sigma_z$  being the Pauli-z operator. The final term represents the interaction between the qubit and the resonator, where  $g$  is the coupling strength and  $\sigma^\pm$  are the qubit raising and lowering operators.

For qubit readout, we operate in the dispersive regime, which is defined by a large detuning between the resonator and qubit frequencies ( $|\Delta| = |\omega_q - \omega_r| \gg g$ ). This regime strongly suppresses the energy exchange between the qubit and resonator. Instead, the interaction produces a coherent resonator frequency shift dependent on the qubit's state. This phenomenon is known as dispersive coupling.

By applying a second-order perturbation theory approximation in terms of  $g/\Delta$ , and in the limit of a few photons in the resonator (known as the dispersive approximation), the JC Hamiltonian can be simplified to a more descriptive, effective Hamiltonian:

$$H_{\text{disp}} = \hbar\omega_r \left( a^\dagger a + \frac{1}{2} \right) + \frac{\hbar}{2} \left( \underbrace{\omega_q + \frac{g^2}{\Delta}}_{\text{Lamb shift}} + \underbrace{\frac{2g^2}{\Delta} a^\dagger a}_{\text{ac-Stark shift}} \right) \sigma_z. \quad (2.5)$$

In the dispersive regime, the approximation leading to Equation (2.5) is only valid when the number of photons in the resonator remains below a certain threshold. This threshold is characterized by the critical photon number, defined as

$$n_{\text{crit, JC}} = \frac{\Delta^2}{4g^2}. \quad (2.6)$$

For photon numbers  $n \ll n_{\text{crit, JC}}$ , the perturbative expansion in  $g/\Delta$  remains valid, and the system is well described by the effective dispersive Hamiltonian. When  $n \gtrsim n_{\text{crit, JC}}$ , higher-order terms become significant.

This effective Hamiltonian reveals the key physical effects of the dispersive interaction. The term  $\frac{g^2}{\Delta}$  represents the Lamb shift, a state-dependent shift of the qubit's frequency due to its coupling to the resonator. The term  $\frac{2g^2}{\Delta} a^\dagger a$  describes the ac-Stark shift, where the resonator's frequency is shifted by an amount that depends on the state of the qubit.

From this, we can define the dispersive shift  $\chi$  as:

$$\chi = \frac{g^2}{\Delta} = \frac{g^2}{\omega_q - \omega_r}. \quad (2.7)$$

In the case where we consider a model with more than two levels:

$$\chi = \frac{g_{01}^2}{\Delta} \left( \frac{1}{1 + \Delta/\alpha} \right). \quad (2.8)$$

The dispersive shift  $\chi$  is the key to qubit readout. By measuring the resonator's frequency with an external signal, one can infer whether the qubit is in the  $|0\rangle$  or  $|1\rangle$  state.

## 2.3 Qubit Readout

The primary goal of qubit readout is to determine the qubit's quantum state without disturbing the measured state. As established in Section 2.2, in circuit cQED, this is achieved through an indirect method known as dispersive readout.

### Dispersive Readout Principle

The principle of dispersive readout is based on the qubit's state, causing a dispersive shift in the readout resonator's frequency, as derived from the effective Hamiltonian in the dispersive regime Equation (2.5), the resonator's frequency is shifted depending on the qubit's state. When the qubit is in  $|0\rangle$ , the effective frequency is  $\omega_{r,|0\rangle} = \omega_r + \chi$ , and when it is in  $|1\rangle$ , it is  $\omega_{r,|1\rangle} = \omega_r - \chi$ . Here,  $\omega_r$  is the bare resonator frequency and  $\chi$  is the dispersive shift. By probing the resonator with a microwave signal at a frequency between these two states, the resulting output signal (reflected or transmitted) will have a different phase and amplitude depending on the resonator state. Measuring these differences enables the inference of the qubit's state.

### Heterodyne Detection and Demodulation

To measure the small changes in the amplitude and phase of the microwave signal, a highly sensitive and precise measurement technique is required. This is accomplished using a method called heterodyne detection, which converts the high-frequency microwave signal into a much lower, more manageable frequency without losing the crucial phase and amplitude information.

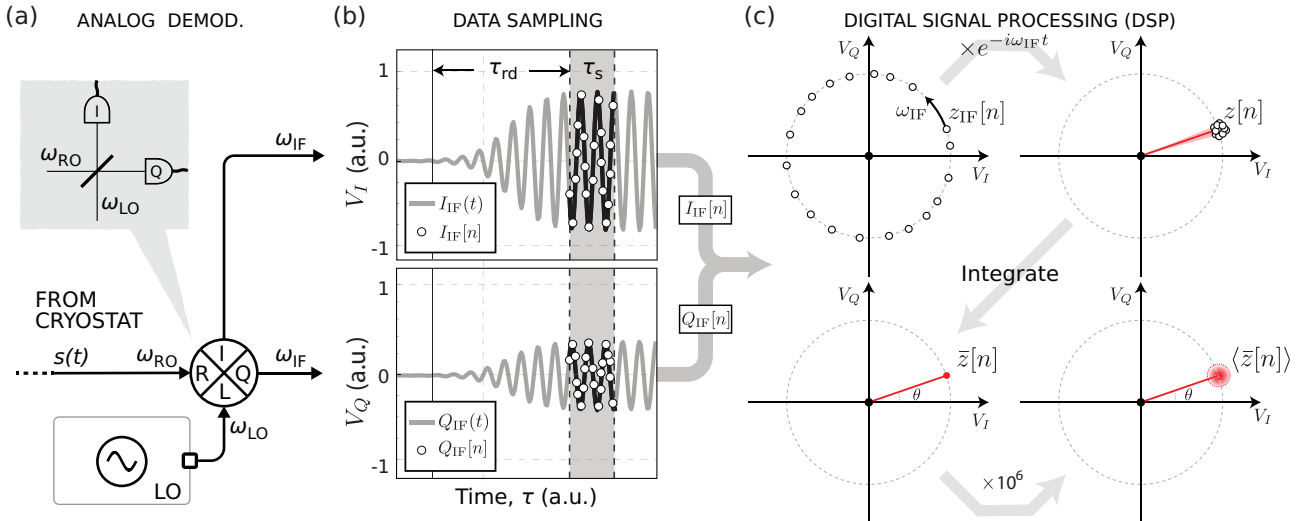


**Figure 2.2** Heterodyne detection schematic. (a) The signal  $s(t)$  at frequency  $\omega_{\text{RF}}$  is mixed with a local oscillator at  $\omega_{\text{LO}}$ , producing two quadratures at intermediate frequency  $\omega_{\text{IF}}$ ,  $90^\circ$  out of phase. (b) Two ADC channels digitize these after a readout delay  $\tau_{\text{rd}}$  and sampling time  $\tau_s$  (white dots show samples). (c) Post-processing yields a single point in the  $(I, Q)$ -plane per shot. Repeating this many times forms a 2D histogram with a Gaussian distribution due to noise. Figure taken from [Kra+19].

The readout pulse after interacting with the resonator (reflected or transmitted) is represented as

$$s(t) = A_{\text{RF}} \cos(\omega_{\text{RF}}t + \theta_{\text{RF}}), \quad (2.9)$$

and it carries information on the qubit's state.

The first step is analog mixing. This signal is mixed with a local oscillator (LO) signal,  $y(t) = A_{\text{LO}} \cos(\omega_{\text{LO}}t)$ , in an I/Q mixer. After low-pass filtering to remove the high-frequency sum component ( $\omega_{\text{RF}} + \omega_{\text{LO}}$ ), the mixer produces two intermediate frequency (IF) signals,  $90^\circ$  out of phase (in quadrature):

$$\begin{aligned} I_{\text{IF}}(t) &= G_{\text{LPF}}[s(t) \cdot y_I(t)] = G_{\text{LPF}}[A_{\text{RF}} \cos(\omega_{\text{RF}}t + \theta_{\text{RF}}) \cdot A_{\text{LO}} \cos(\omega_{\text{LO}}t)] \\ &= G_{\text{LPF}}\left[\frac{A_{\text{RF}}A_{\text{LO}}}{2} [\cos((\omega_{\text{RF}} + \omega_{\text{LO}})t + \theta_{\text{RF}}) + \cos((\omega_{\text{RF}} - \omega_{\text{LO}})t + \theta_{\text{RF}})]\right] \\ &= A_{\text{IF}} \cos(\omega_{\text{IF}}t + \theta_{\text{RF}}), \end{aligned} \quad (2.10)$$

$$\begin{aligned} Q_{\text{IF}}(t) &= G_{\text{LPF}}[s(t) \cdot y_Q(t)] = G_{\text{LPF}}[A_{\text{RF}} \cos(\omega_{\text{RF}}t + \theta_{\text{RF}}) \cdot (-A_{\text{LO}} \sin(\omega_{\text{LO}}t))] \\ &= G_{\text{LPF}}\left[\frac{A_{\text{RF}}A_{\text{LO}}}{2} [-\cos((\omega_{\text{RF}} + \omega_{\text{LO}})t + \theta_{\text{RF}}) + \sin((\omega_{\text{RF}} - \omega_{\text{LO}})t + \theta_{\text{RF}})]\right] \\ &= A_{\text{IF}} \sin(\omega_{\text{IF}}t + \theta_{\text{RF}}), \end{aligned} \quad (2.11)$$

where  $A_{\text{IF}}$  is the new IF amplitude, proportional to  $A_{\text{RF}}A_{\text{LO}}$  and  $G_{\text{LPF}}$  denotes the low-pass filtering operation. The intermediate frequency is the difference between the RF and LO frequencies,  $\omega_{\text{IF}} = \omega_{\text{RF}} - \omega_{\text{LO}}$ .

Following this analog down-conversion, the IF signal is digitized by the analog-to-digital converters (ADCs). The digital signal is then demodulated to extract the in-phase (I) and quadrature (Q) components, which form the basis for qubit state discrimination. This is achieved by numerically multiplying the digitized complex signal with a complex reference oscillator at the IF,  $e^{-i\omega_{\text{IF}}t}$ :

$$\begin{aligned} z(t) &= Z_{\text{IF}}(t) \cdot e^{-i\omega_{\text{IF}}t} \\ &= \left(A_{\text{IF}}e^{i(\omega_{\text{IF}}t + \theta_{\text{RF}})}\right) \cdot e^{-i\omega_{\text{IF}}t} \\ &= A_{\text{IF}}e^{i\theta_{\text{RF}}} = A_{\text{IF}}(\cos(\theta_{\text{RF}}) + i \sin(\theta_{\text{RF}})). \end{aligned} \quad (2.12)$$

The result,  $z(t)$ , is a complex number that is now constant in time (DC), holding the amplitude and phase information of the original RF signal. To obtain a single measurement point and average out high-frequency noise, this signal is integrated over a measurement duration  $\tau_s$ :

$$I = \text{Re} \left[ \frac{1}{\tau_s} \int_0^{\tau_s} z(t) dt \right] = A_{\text{IF}} \cos(\theta_{\text{RF}}), \quad (2.13)$$

$$Q = \text{Im} \left[ \frac{1}{\tau_s} \int_0^{\tau_s} z(t) dt \right] = A_{\text{IF}} \sin(\theta_{\text{RF}}). \quad (2.14)$$

The final  $I$  and  $Q$  values represent a single point in a two-dimensional plane. Due to noise, repeated measurements of the same qubit state will not yield the same point, but will instead form a cluster with generally a Gaussian distribution.

The goal of the readout algorithm is to classify each measured  $(I, Q)$  point as either the ground state ( $|g\rangle$ ) or the excited state ( $|e\rangle$ ). This is achieved by training a classification model, such as a Linear Discriminant Analysis (LDA) classifier, on a set of known ground and excited state measurements. The classifier learns to draw an optimal boundary in the  $I - Q$  plane, maximizing the separation between the two state clusters. The distinguishability of these clusters is quantified by the signal-to-noise ratio (SNR). The signal here is the distance between the centers of the two clusters, which depends on detuning  $\Delta$  (Equation (2.8)), while the noise is their spread.

The SNR for a measurement integrated over a time  $\tau_m$  is formally defined as:

$$\text{SNR}^2(\tau_m) \equiv \frac{|\langle \hat{M}(\tau_m) \rangle_e - \langle \hat{M}(\tau_m) \rangle_g|^2}{\langle \hat{M}_N^2(\tau_m) \rangle_e + \langle \hat{M}_N^2(\tau_m) \rangle_g}, \quad (2.15)$$

where  $\langle M(\tau_m) \rangle_\sigma$  is the average integrated signal for the given qubit in state  $\sigma$ , and  $\hat{M}_N$  is the noise operator. A high SNR is crucial for reliable classification.

The accuracy of this classification determines the measurement fidelity ( $F_m$ ), which is defined by the probabilities of correct and incorrect state assignments. It is given by:

$$F_m \equiv 1 - [P(e|g) + P(g|e)] \equiv 1 - E_m, \quad (2.16)$$

where  $P(\sigma|\sigma')$  is the probability of measuring a qubit in state  $\sigma$  when it was actually prepared in state  $\sigma'$  and  $E_m$  is the measurement error. From the I-Q plot,  $E_m$  is calculated as the fraction  $\frac{N_{\text{err}}}{N_{\text{tot}}}$ , using the total number of measurements ( $N_{\text{tot}}$ ) and the number of incorrectly classified outcomes ( $N_{\text{err}}$ ).

If the measurement outcomes have a Gaussian distribution, the fidelity is directly related to the SNR by the complementary error function

$$F_m = 1 - \text{erfc}(\text{SNR}/2). \quad (2.17)$$

### 2.3.1 S-Parameters

As described previously, the readout process relies on measuring the amplitude and phase of a microwave signal after it has interacted with the resonator. To mathematically model the readout signal's interaction with the resonator, we use scattering parameters (S-parameters), which describe the relation of the waves' amplitudes leaving the ports of a network to the amplitudes of waves entering them.

For example, the  $S_{21}$  parameter describes the transmission from port 1 to port 2. The theoretical function for the  $S_{21}$ -parameter of the resonator as described by Khalil et al. [Kha+12] is given by

$$S_{21}(f) = 1 - \frac{Q Q_e^{-1}}{1 + 2jQ(f - f_0)/f_0}, \quad (2.18)$$

where  $f_0$  is the frequency of the resonator,  $Q$  and  $Q_e$  are the total and external quality factors.

## 2.4 Measurement-Induced State Transitions (MISTs)

For fast and reliable qubit measurements, a major problem is the effect of Measurement-Induced State Transitions (MISTs), also known as "transmon ionization" [Dum+24]. This occurs when a powerful measurement signal, intended for a high-fidelity readout, induces unwanted transitions in the qubit from its computational states ( $|0\rangle$  or  $|1\rangle$ ) to higher, non-computational energy levels. These transitions are one of the main reasons for the failure of a measurement to be QND and can significantly reduce the processor's operability.

To understand these transitions, we first consider the full quantum model of the combined qubit-resonator system. In this model, the state is described by a state  $|\overline{i_t, n_r}\rangle$ , where  $i_t$  is the transmon's energy level and  $n_r$  is the photon number in the resonator. The full quantum Hamiltonian for this coupled system is:

$$\hat{H} = \hbar\omega_r a^\dagger a + \hat{H}_t + \hat{H}_{\text{int}}.$$

Here,  $\hat{H}_t = 4E_C(\hat{n}_t - n_g)^2 - E_J \cos(\hat{\phi}_t)$  is the transmon Hamiltonian, discussed in Section 2.1,  $\hbar\omega_r a^\dagger a$  is the resonator Hamiltonian, and  $\hat{H}_{\text{int}} = -i\hbar g(\hat{n}_t - n_g)(a - a^\dagger)$  is the capacitive interaction term. The term  $n_g$  in  $\hat{H}_t$ , as discussed in Section 2.1, represents the offset charge on the transmon's capacitor island, a superconducting

electrode in the transmon qubit, that is part of the capacitor and is connected to the Josephson junction. While the computational states  $|0\rangle$  and  $|1\rangle$  are designed to be insensitive to fluctuations in  $n_g$  (due to  $E_J/E_C \gg 1$ ), MISTs fundamentally involve transitions to high-energy transmon states. These higher-energy states, however, are not insensitive to charge and exhibit significant charge dispersion. Consequently, fluctuations in gate charge can shift these high-energy levels, which makes the critical photon number for ionization dependent on gate charge noise. That's why it is important to include  $n_g$  for a more accurate theoretical model.

The eigenstates of this coupled system can be organized into "branches", where each branch  $B_i$  is labeled by a specific bare transmon state  $|i_t\rangle$  at zero resonator photons ( $n_r = 0$ ). The branches are then built recursively, where for a given state in the branch at photon number  $n_r$ , the next state at  $n_r + 1$  is found by selecting the candidate's eigenstate,  $|\lambda\rangle$ , that maximizes the overlap  $|\langle\lambda|\hat{a}^\dagger|i_t, n_r\rangle|^2$ . An ideal QND measurement implies that the system's dynamics are confined to a single branch. However, under a strong drive, the average transmon population within two branches can be exchanged, a process illustrated in Figure 2.3. This exchange, for example, where the average transmon population of branch  $B_{1_t}$  swaps with that of branch  $B_{7_t}$  and vice-versa, causes the qubit to move out of the computational subspace.

A key reason for these inter-branch transitions is the presence of "avoided crossings" in the energy spectrum. This phenomenon occurs when a multi-photon resonance condition is met:

$$E_j - E_i \approx k\hbar\omega_d \quad \text{with } k \in \mathbb{Z}, \quad (2.19)$$

where  $E_i$  and  $E_j$  are the energies of two dressed states,  $\omega_d$  is the drive frequency.

The dynamics of traversing the resonance can be described by the Landau-Zener model, which gives us the transition probability  $P_{LZ} = \exp(-\pi\Delta_{ac}^2/2v)$ , where  $\Delta_{ac}$  is the energy gap at the avoided crossing and  $v$  is the speed of passage through the resonance. A slow passage allows the system to remain on its energy curve, corresponding to an *adiabatic transition* into the higher-energy, ionized state. Conversely, a rapid passage can cause the system to "jump" the gap and remain in a state of similar character, a process known as a *diabatic transition*, thus avoiding ionization. The measurement pulse shape, which dictates this passage speed, is therefore critical in determining the probability of MISTs.

### 2.4.1 Semiclassical Analysis

While the full quantum model described in Section 2.4 provides a complete picture of the qubit-resonator system, its simulation is computationally intensive, especially when exploring a large parameter space. To efficiently predict the critical photon number above which MISTs are likely to occur, the semiclassical model proposed by Dumas et al. [Dum+24] can be used. This approach simplifies the problem by treating the driven resonator not as a quantum object, but as a classical, time-periodic drive acting on the transmon qubit, and a comparison with a fully quantum model (Section 2.4), shown in Figure 2.4, reveals that both approaches yield nearly identical predictions.

In this model, the system is described by the time-dependent Hamiltonian:

$$\hat{H}(t) = \hat{H}_t + \mathcal{E}_t(t)\hat{n}_t, \quad (2.20)$$

where  $\hat{H}_t = 4E_C(\hat{n}_t - n_g)^2 - E_J \cos(\hat{\phi}_t)$  is the full transmon Hamiltonian as in Section 2.1, and the term  $\mathcal{E}_t(t)\hat{n}_t$  represents the classical drive on the transmon. For resonator drive frequency  $\omega_d$  close to the resonator frequency  $\omega_r$  we can use approximation  $\mathcal{E}_t(t) \approx \varepsilon_t(t) \cos(\omega_d t)$  with  $\varepsilon_t(t) \approx 2\hbar g\sqrt{n_r}$  as the time-dependent amplitude. This establishes a direct link between the strength of the classical drive and the resonator photon number, which is a key experimental parameter.

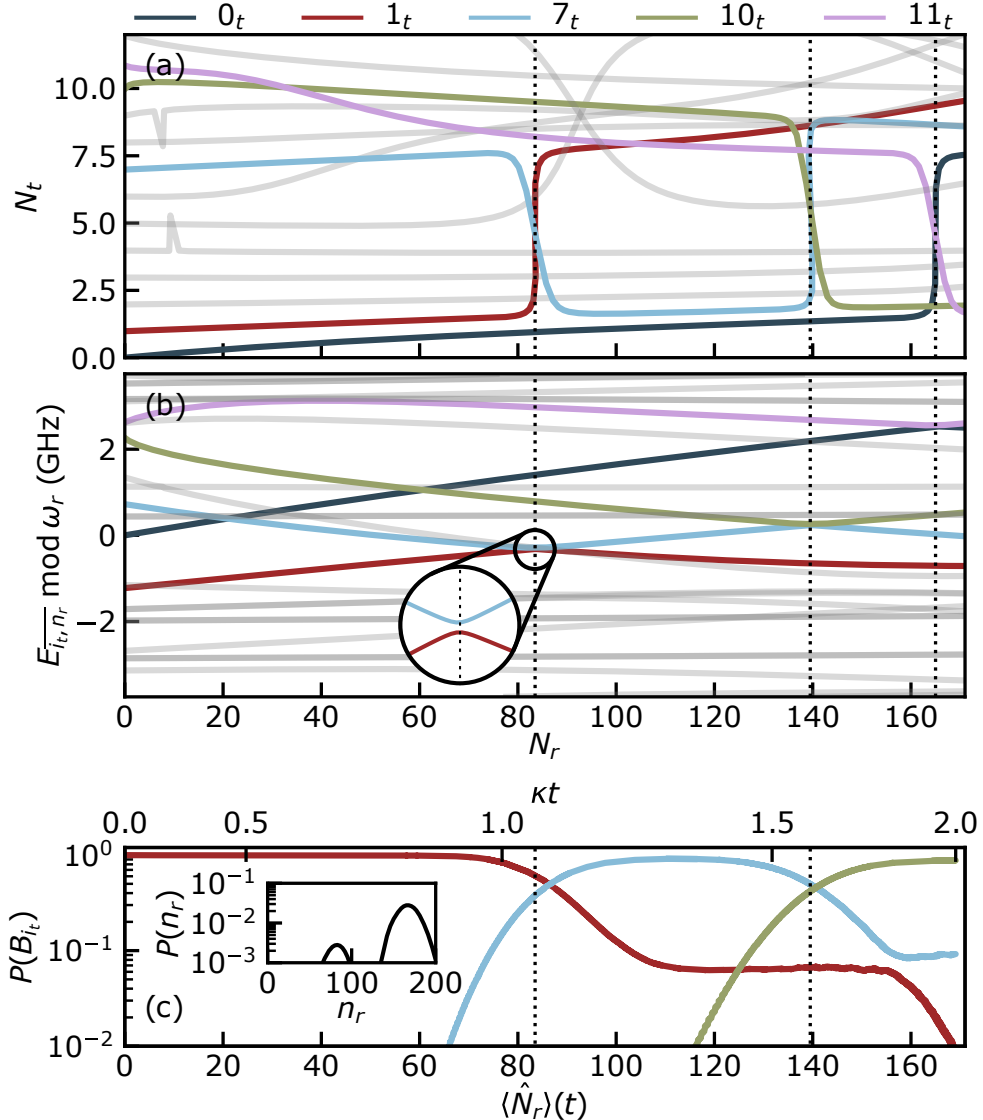


**Figure 2.3** Branch analysis for a transmon-resonator system at negative detuning ( $\omega_q < \omega_r$ ). (a) The average transmon population  $N_t$  for each branch shows an abrupt "swapping" of character between branches (e.g., between  $B_{1_t}$  and  $B_{7_t}$ ) at specific resonator photon numbers  $N_r$ . (b) This swapping corresponds to avoided crossings in the energy spectrum of the system, shown here folded modulo  $\omega_r$ . The dotted lines mark the photon numbers where these strong interactions occur. (c) Dynamics of the driven transmon-resonator system when initializing in the excited state  $|1_t, 0_r\rangle$ . Figure taken from [Dum+24].

### Floquet's Theorem and Quasienergies

Because  $\varepsilon_t(t) \propto \sqrt{\bar{n}_r(t)}$  changes on a timescale  $1/\kappa \gg T = 2\pi/\omega_d$ , we can set  $\varepsilon_t(t)$  to be constant and the Hamiltonian is periodic in time,  $\hat{H}(t) = \hat{H}(t + T)$ , so that the instantaneous Floquet spectrum can be used. Floquet's theorem provides a powerful framework for analyzing the dynamics of periodic Hamiltonians. The theorem states that the solutions to the Schrödinger equation can be written in the form of Floquet modes,  $|\phi_{i_t}(t)\rangle$ , which are periodic eigenstates of the driven system, and associated with each mode quasienergies,  $\epsilon_{i_t}$ , which are the effective energies of the corresponding states in the presence of the drive.

It's important to mention that quasienergies are only defined modulo the drive frequency,  $\epsilon_{i_t} \equiv \epsilon_{i_t} + k\hbar\omega_d$ , where  $k$  is an integer. This folding of the energy spectrum into a single Brillouin zone of width  $\hbar\omega_d$  is a

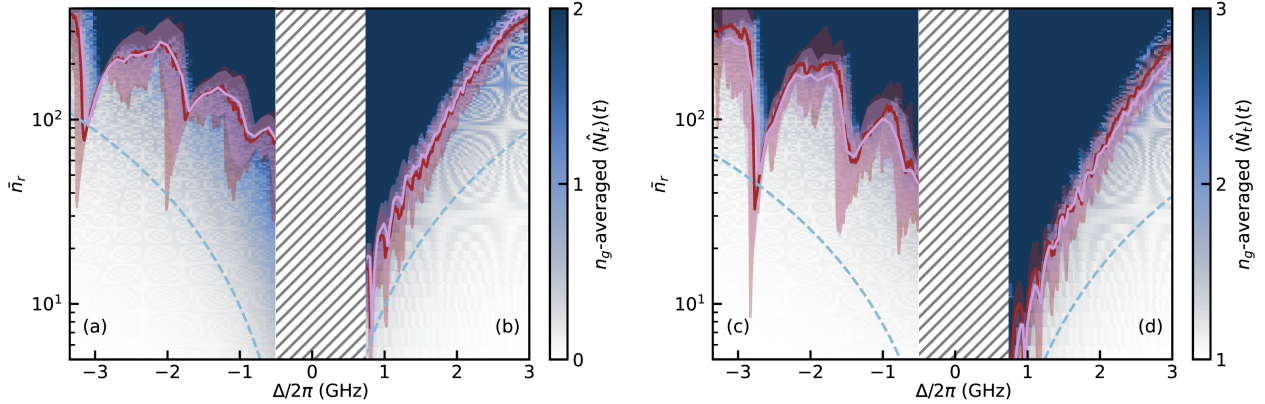


**Figure 2.4** Critical photon number for ionization as a function of detuning, adapted from [Dum+24]. The plots show the threshold for the (a, b) ground and (c, d) excited states. The colored background represents the final transmon population from time-dynamics simulations. The overlaid lines show the critical photon number that the full quantum model (pink) and the semiclassical Floquet model (red) predicted. The agreement between the two models is excellent.

central feature of the model. It allows energy levels that are far apart in the undriven system to become nearly degenerate in the driven system, leading to the avoided crossings responsible for MISTs.

## 2.5 Relating Input Power to Photon Number

We model the dynamics of the resonator's state amplitude,  $\alpha(t)$ , using the semiclassical input-output theory for a driven, damped harmonic oscillator [Bla+21, Sec. V.C]. The equation of motion, also known as the Langevin equation, is given by:

$$\frac{d\alpha(t)}{dt} = -i\varepsilon_d(t) - \left(\frac{\kappa}{2} + i(\omega_r - \omega_d \mp \chi)\right)\alpha(t), \quad (2.21)$$

where  $\kappa$  is the total energy decay rate of the resonator (linewidth),  $\omega_r$  is its bare resonator frequency,  $\omega_d$  is the drive frequency, and  $\chi$  is the dispersive shift. The sign of  $\chi$  depends on whether the qubit is in the ground ( $|g\rangle$ ) or excited ( $|e\rangle$ ) state.

The time-dependent amplitude of the drive as seen by the resonator mode,  $\varepsilon_d(t)$ , is related to the amplitude of the input field,  $A(t)$ , as  $\varepsilon(t) = i\sqrt{\kappa_{\text{ext}}}A(t)$  [Bla+21, Sec. IV.F], where  $\kappa_{\text{ext}}$  is the external coupling rate of the resonator to the feedline. Also  $P_{\text{in}}(t) = \hbar\omega_d\langle b_{\text{in}}(t)b_{\text{in}}^\dagger(t)\rangle$  [Cle+10, Appx. E.2], where the operator  $\hat{b}_{\text{in}}(t)$  represents the classical drive. Because  $\langle \hat{b}_{\text{in}}(t)\hat{b}_{\text{in}}^\dagger(t)\rangle = |A(t)|^2$  we can write the input power  $P_{\text{in}}$  at the resonator port as

$$|\varepsilon_d(t)|^2 = \kappa_{\text{ext}}|A(t)|^2 = \frac{P_{\text{in}}(t)\kappa_{\text{ext}}}{\hbar\omega_d}. \quad (2.22)$$

For a square readout pulse of constant power,  $\varepsilon_d(t) = \varepsilon_d$  for  $t > 0$ . The Langevin equation simplifies to a first-order linear ordinary differential equation:

$$\frac{d\alpha(t)}{dt} + \left(\frac{\kappa}{2} + i\Delta_{d,g/e}\right)\alpha(t) = -i\varepsilon_d, \quad (2.23)$$

where  $\Delta_{d,g/e} = \omega_r - \omega_d \mp \chi$  is the detuning of the drive from the qubit-state-dependent resonator frequency. Assuming the resonator starts in the vacuum state ( $\alpha(0) = 0$ ), the solution to this equation is:

$$\alpha(t) = \underbrace{\frac{-i\varepsilon_d}{\kappa/2 + i\Delta_{d,g/e}}}_{\alpha_{\text{ss}}} \left(1 - e^{-(\kappa/2 + i\Delta_{d,g/e})t}\right). \quad (2.24)$$

## 2 Theoretical Background

The term  $\alpha_{ss}$  represents the steady-state amplitude that the resonator field would reach for a continuous drive. The exponential term describes the transient build-up of the field inside the resonator, which occurs on a timescale of  $1/\kappa$ .

The time-dependent photon number in the resonator is given by  $n(t) = |\alpha(t)|^2$ . Using Equation (2.24) and Equation (2.22), we arrive at the central relationship connecting input power to photon number:

$$n(t) = |\alpha_{ss}|^2 \cdot \left| 1 - e^{-(\kappa/2+i\Delta_{d,g/e})t} \right|^2 \quad (2.25)$$

$$= \frac{P_{in}\kappa_{ext}/(\hbar\omega_d)}{(\kappa/2)^2 + \Delta_{d,g/e}^2} \cdot \left| 1 - e^{-(\kappa/2+i\Delta_{d,g/e})t} \right|^2. \quad (2.26)$$

This equation forms the bridge between our two simulations. It allows us to calculate the maximum photon number,  $n_{max} = n(t_p)$ , reached at the end of a pulse of duration  $t_p$  for a given input power  $P_{in}$  and detuning.

The behaviour described by Equation (2.26) is visualized in Figure 2.5. The left top panel shows the characteristic build-up of photons inside the resonator over the duration of the readout pulse. The bottom left panel illustrates that for a fixed input power and pulse frequency, the maximum number of photons we can get into the resonator is strongly dependent on the qubit-resonator detuning,  $\Delta$ .

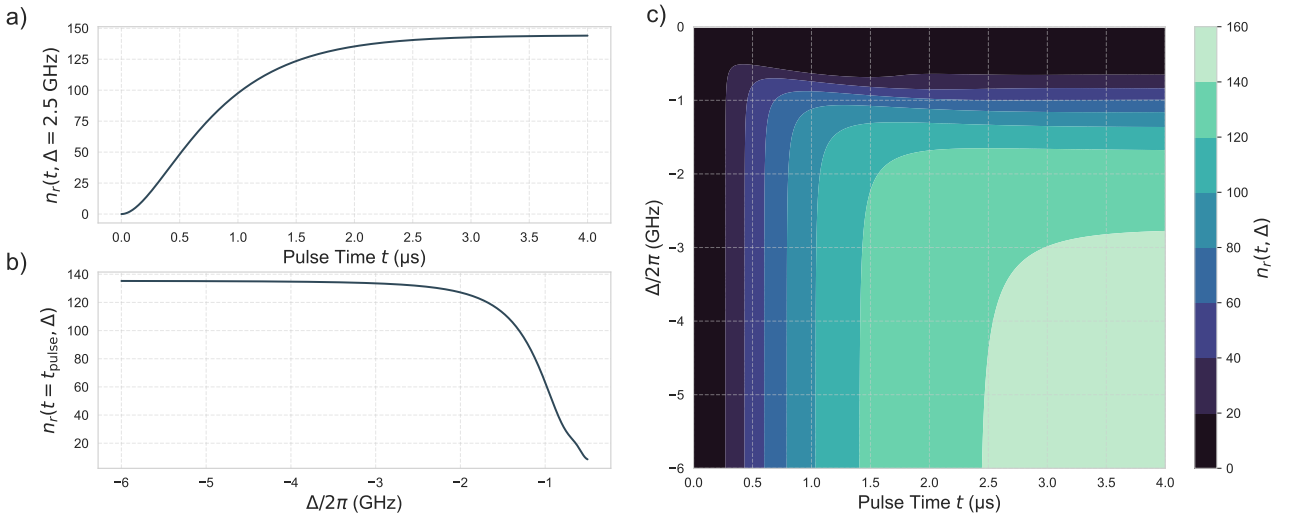


**Figure 2.5** Simulated intracavity ( $\kappa/2\pi = 0.55$  MHz) photon number based on Equation (2.26) during a square readout pulse of length  $t$  with a fixed input power  $P_{in} = -123$  dBm (a) Photon number built up over time,  $n_r(t)$ . The resonator populates on a timescale determined by its decay rate  $\kappa$ . (b) The maximum photon number reached at the end of the pulse,  $n_{r,max} = n_r(t_{pulse} = 2 \mu s)$ , as a function of the qubit-resonator detuning  $\Delta/2\pi$ . For a fixed input power and drive frequency, the efficiency of populating the resonator is highly dependent on the detuning from the pulled resonance frequency, leading to a strong dependence of  $n_{r,max}$  on  $\Delta$ . (c) Built up photon number in dependence of time  $t$  and detuning  $\Delta/2\pi$ .

# 3 Methodology

As mentioned in Chapter 1, the main goal of the thesis is to draw a conclusion on whether it is reasonable to use high-frequency resonators, such that the detuning of the resonator-qubit system is large enough to mitigate MISTs. However, using highly detuned systems can also affect the fidelity negatively, as the SNR also depends on detuning (Section 2.3). All subsequent calculations are based on the measurement data in Table 1, including the  $S_{21}$  spectra from Appendix A, unless stated otherwise. For the readout, we use a square pulse with a carrier frequency set to the average of the two state-dependent resonator frequencies:  $\omega_d = (\omega_{r,|0\rangle} + \omega_{r,|1\rangle})/2$ . This choice, which places the frequency exactly between the values for the ground and excited states, is considered optimal for state discrimination [Kra+19].

## 3.1 Fidelity Simulation Framework

In this section, we detail a simple simulation framework that models the readout process of a transmon qubit in cQED, from the input pulse to the final measurement, allowing us to explore the readout fidelity dependence on detuning.

### 3.1.1 Core Methodology

At first, we implement the fidelity simulation based on the approach from [Won+23], where electromagnetic modeling in Ansys HFSS [Ans24] was combined with signal and noise modeling in MATLAB. Our implementation adapts this methodology using Python for the simulation framework. The framework is designed to co-optimize the resonator design, qubit-resonator coupling, and readout pulse characteristics with noise considerations, as illustrated in Figure 3.1b.

The methodology begins with Ansys HFSS [Ans24], which is used to perform the S-parameter (Section 2.3.1) simulation of the resonator based on the measured or calculated dispersive shift,  $\chi$ , and the design of the resonator.

The measured or specified input pulse  $V_{\text{in}}(t)$  is transformed to the frequency domain via a Fast Fourier Transform (FFT) to obtain  $V_{\text{in}}(f)$ . The resonator output is calculated as

$$V_{\text{out}}(f) = S_{21}(f) \cdot V_{\text{in}}(f), \quad (3.1)$$

which sets the signal amplitude before noise is added. The readout path (Figure 3.1a) includes three attenuation stages (-60 dB total), cables (-16 dB), and three amplification stages: a Traveling Wave Parametric Amplifier (TWPA) (+20 dB), a High Electron Mobility Transistor (HEMT) amplifier (+40 dB), and a 300 K amplifier (+40 dB). White noise sources are generated in MATLAB to model quantum noise and noise from amplifiers.

### 3 Methodology

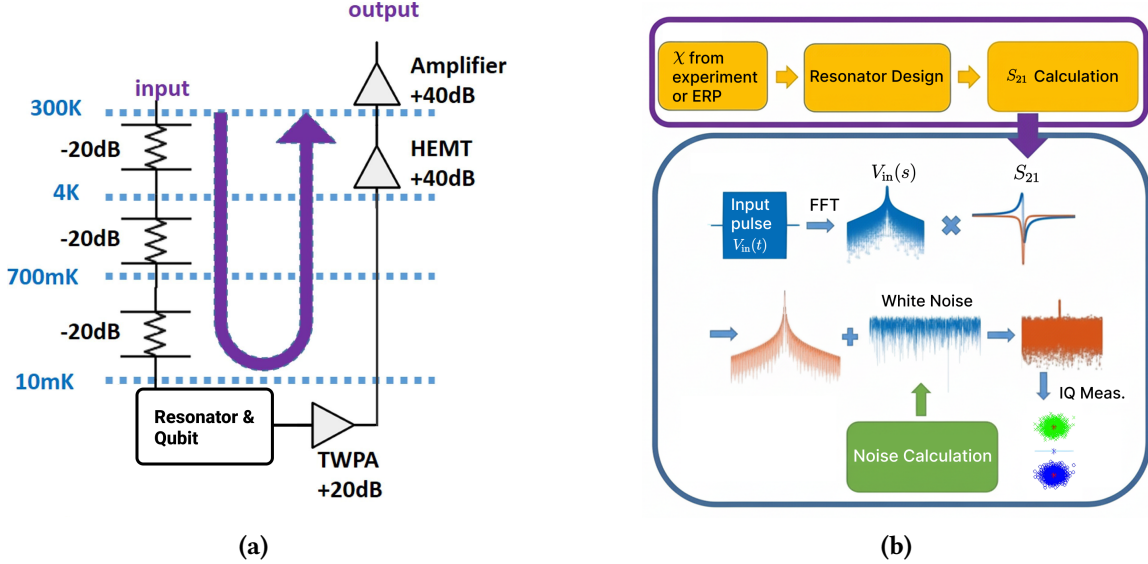


**Figure 3.1** (a) The qubit system and the readout path with all three amplification stages, which contributed to the considered noise. (b) Simulation methodology for superconducting qubit readout fidelity, combining resonator modeling with noise and signal simulation. Adapted from [Won+23].

#### Noise Modeling

The most important part in the simulation is the accurate modeling of noise, which determines the size of the clusters on the IQ-Plane and fidelity. We consider here the quantum noise due to the photon number fluctuation and coming from the TWPA, and thermal noise from the HEMT and 300 K amplifier.

The Quantum noise temperature given by

$$T_n = \frac{hf}{k \ln 2}, \quad (3.2)$$

where  $h$  is Planck's constant,  $f$  the readout frequency, and  $k$  Boltzmann's constant. The thermal noise spectral density is calculated as

$$N_{\text{th}} = 4kT_{\text{eff}}R \quad (3.3)$$

with  $R = 50 \Omega$ ,  $T_{\text{eff}} = 1.5 \text{ K}$  for the HEMT and  $T_{\text{eff}} = 54 \text{ K}$  for 300 K amplifier. The total mean-square noise voltage over an effective bandwidth  $B$  is  $\langle V_{\text{noise}}^2 \rangle = N_{\text{th}} \cdot B$ . The corresponding root-mean-square (RMS) voltage amplitude is therefore

$$V_{\text{noise, RMS}} = \sqrt{N_{\text{th}} \cdot B} = \sqrt{4kT_{\text{eff}}RB}, \quad (3.4)$$

with  $B = 1/t_p$  for quantum noise and fixed values (e.g., 6 GHz) for amplifier thermal noise. All noise is generated in the time domain, transformed to the frequency domain, and combined with the signal. The noisy output is then processed to extract the in-phase (I) and quadrature (Q) components at the readout frequency, simulating a quadrature measurement. Randomized noise realizations produce I-Q distributions for both qubit states, from which the fidelity  $F_m$  is computed (see Equation (2.16)).

#### 3.1.2 Our Implementation and Key Additions

##### S-Parameters

As mentioned in Section 3.1.1, the S-parameters of the system are a key component of the methodology. Originally, these were intended to be simulated using Ansys software, following the strategy outlined in the referenced paper [Won+23]. However, we found this approach to be suboptimal. The primary reason was that the simulations for a single resonator system were neither precise nor efficient enough. The simulated

S-parameter peaks were significantly shifted due to an insufficiently dense mesh (Figure 3.2b), a problem that would require substantial computing power and time to resolve.

For our purposes, we determined that it was more practical and efficient to use the theoretical function for the  $S_{21}$ -parameter of the resonator (Equation (2.18)). This analytical approach not only bypasses the computational challenges of electromagnetic simulations but also provides a flexible and efficient means to explore the parameter space for different detunings, which is essential for the scope of this thesis.

For a more direct comparison to experimental results or better predictions, the experimentally obtained  $S_{21}$  spectra can be utilized, which can also be shifted to simulate different detunings.

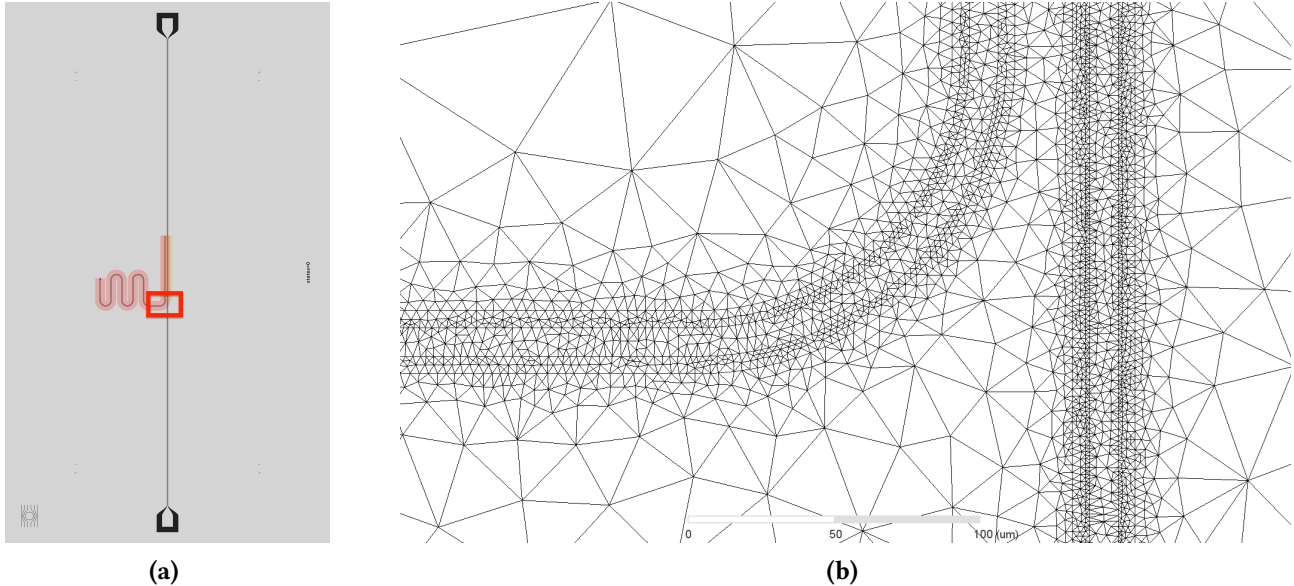


**Figure 3.2** (a) Chip design for S-parameter simulation of the  $|0\rangle$  state. The red rectangle highlights the region shown in (b). (b) A close-up of the finite element mesh used during the simulation, illustrating the mesh density.

## IQ Projection

The final step in the simulation is the IQ projection, which converts the signal into its in-phase (I) and quadrature (Q) components for later analysis and fidelity estimation. In [Won+23], this was performed in the frequency domain by taking the imaginary and real parts of the signal at the readout frequency. However, we decided to use a different approach that more closely resembles the actual experimental approach, which is described in Section 2.3, providing theoretically a more realistic representation of the measured I-Q distributions.

### Comparison to [Won+23] Simulation

To confirm that our simulation functions as expected, we used the system and pulse parameters from [Won+23] to compare the relative distance between the blobs on the IQ-plane. The results (Section 3.1.2) appeared similar, with the difference that the centroids in [Won+23] are located at the same  $I$ , which can be either explained by a more simplified method of performing IQ projection or an additional rotation in the post-processing step.

### 3.1.3 Analysis of Readout Fidelity versus Qubit-Resonator Detuning

To demonstrate the capabilities of this framework in Section 3.1.1, we first analyze the fundamental relationship between readout fidelity and qubit-resonator detuning at a fixed power. We calculated the readout

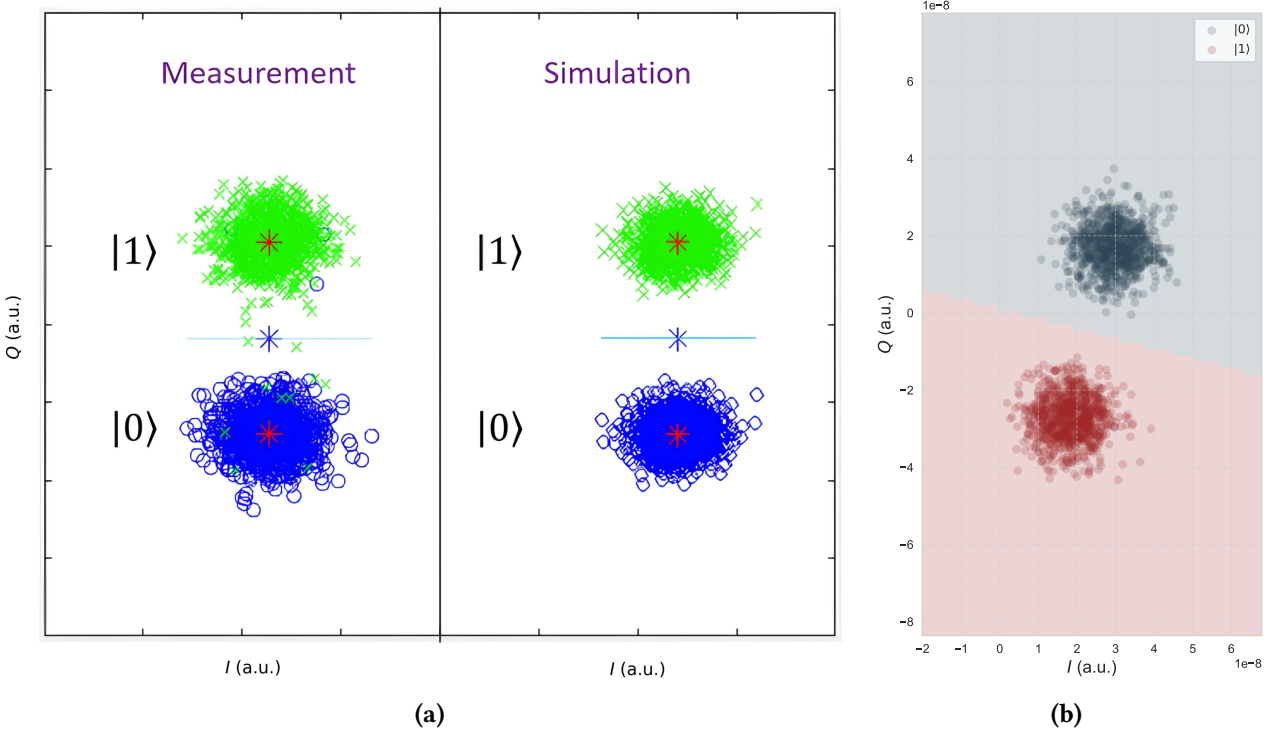


**Figure 3.3** Simulations for reading  $|0\rangle$  and  $|1\rangle$  states with the following parameters:  $f_r = 7.252534$  GHz,  $\frac{\chi}{2\pi} = 156$  kHz,  $Q \approx 48 \cdot 10^3$ ,  $t_{\text{rect. pulse}} = 3.5$   $\mu$ s,  $P_{\text{attenuated}} = -123$  dBm (see Appendix A) (a) Comparison between measurement and simulation of the system fidelity. Adapted from [Won+23]. (b) Our simulation of the system readout fidelity.

fidelity for various detuning values,  $\Delta = \omega_q - \omega_r$ , with a fixed readout power of  $-47$  dBm (attenuated  $-123$  dBm). The results in Figure 3.4a show a non-monotonic relationship, which can be understood by considering two key requirements for high-fidelity dispersive measurements: state distinguishability and sufficient signal strength from the readout pulse. The dispersive shift,  $\chi$ , which separates the qubit states, is approximately  $\chi \approx g^2/\Delta$  (Equation (2.8)).

#### Large Detuning ( $|\Delta/2\pi| > 4$ GHz)

When the qubit is far detuned from the resonator, the large  $|\Delta|$  results in a very small dispersive shift  $\chi$ . Consequently, the frequency separation  $2\chi$  is less than the resonator linewidth ( $\kappa \approx 0.55$  MHz). For example, at  $\Delta/2\pi = -5.5$  GHz, the  $S_{21}$  resonance peaks for state  $|0\rangle$  and  $|1\rangle$  are nearly superimposed. While the readout pulse effectively drives the resonator near its bare frequency  $\omega_r$ , the indistinguishable signals for both states lead to a very low SNR and poor readout fidelity.

#### Optimal Detuning Window (-3.2 to -1.8 GHz)

As  $|\Delta|$  decreases, the dispersive shift  $\chi$  increases, achieving an optimal balance between state distinguishability and efficient resonator driving. This culminates in a maximized SNR and, as seen in our simulations, a broad plateau of high readout fidelity. Within this optimal window, from approximately  $-3.2$  to  $-1.8$  GHz, the frequency separation  $|2\chi|$  is large enough to resolve the states, while the shifted resonator frequencies,  $\omega_r \pm \chi$ , still overlap sufficiently with the readout pulse's spectrum to generate a strong signal.

This behaviour is consistent with established theory. While the ideal steady-state (long-time) limit predicts a sharp optimal SNR at  $|2\chi| = \kappa$  [Bla+21, Eq. (119)], for finite-duration pulses the optimum shifts to a regime

where  $|2\chi| > \kappa$  [Bla+21, Fig. 18(d)]. The theoretical steady-state optimum for our device parameters (Table 1) corresponds to a detuning of  $\Delta/2\pi \approx -2.91$  GHz which is within the observed high-fidelity plateau.

### Small Detuning ( $|\Delta/2\pi| < 1.5$ GHz)

In this regime, the qubit is tuned very close to the resonator, leading to a very large dispersive shift  $\chi$ . For example, at  $\Delta/2\pi = -0.5$  GHz,  $2\chi \approx 13.5$  MHz, indicating excellent state distinguishability. However, the readout fidelity sharply declines. This is because the shifted resonator frequencies,  $\omega_r \pm \chi$ , are now far from the fixed central frequency of the readout pulse. These frequencies fall onto the low-power side lobes of the pulse spectrum. As a result, the resonator is driven with insufficient power, yielding an extremely weak signal for both states that is lost in noise. Thus, despite high intrinsic distinguishability, the lack of sufficient signal strength drastically reduces fidelity.

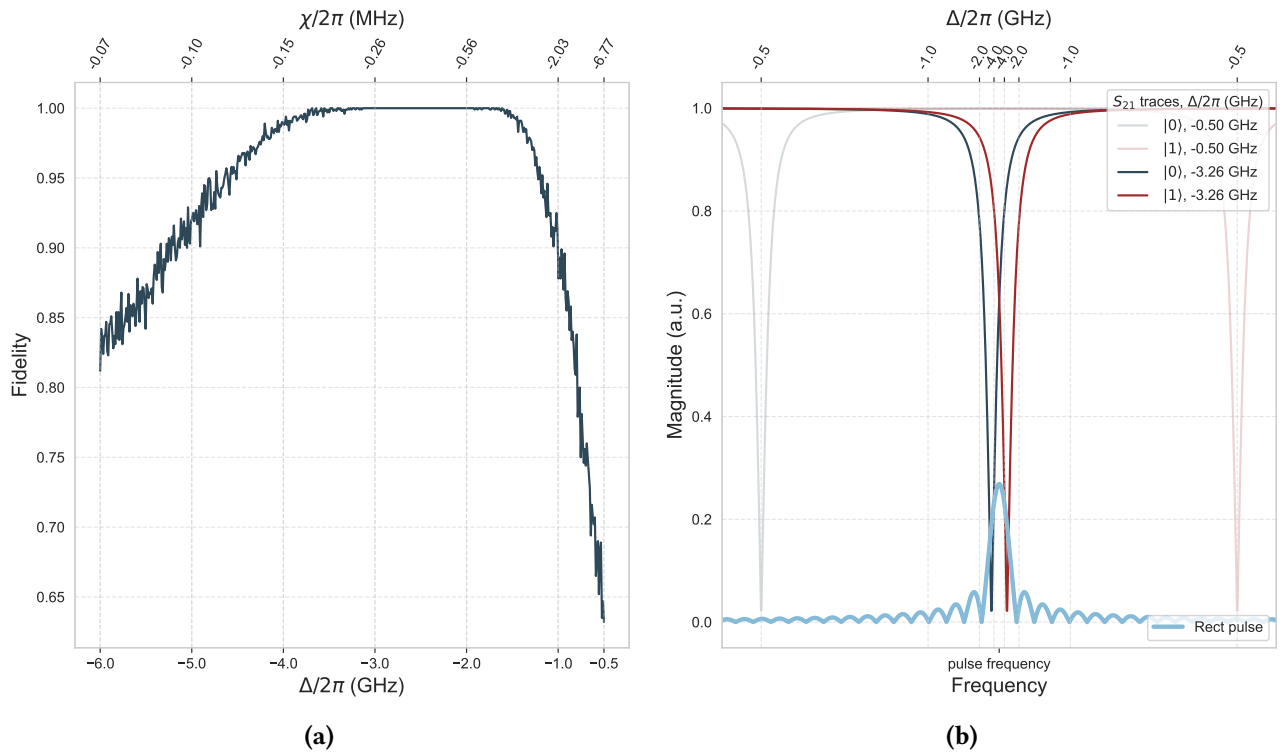


**Figure 3.4** Readout fidelity in dependence on  $\Delta$ . (a) Readout fidelity versus qubit-resonator detuning ( $\Delta/2\pi$ ), with the corresponding dispersive shift ( $\chi/2\pi$ ) shown on the top x-axis. The fidelity exhibits a clear peak at an optimal detuning. (b) Representative  $S_{21}$  spectra for qubit states  $|0\rangle$  (blue) and  $|1\rangle$  (red), illustrating the resonator's magnitude response at two different detunings:  $\Delta/2\pi = -0.5$  GHz (small detuning, large  $\chi$ ) and  $\Delta/2\pi = -5.5$  GHz (large detuning, small  $\chi$ ). The black curve indicates the fixed spectrum of the scaled rectangular readout pulse. These plots collectively explain the non-monotonic fidelity behaviour, demonstrating the critical trade-off between state distinguishability (separation of blue and red curves, proportional to  $\chi$ ) and signal strength (overlap of these curves with the readout pulse). Maximum fidelity is achieved at intermediate detunings where both distinguishability and signal strength are optimized.

## 3.2 MIST Prediction Framework

The core of the framework involves tracking the Floquet quasienergies (Section 2.4.1) as a function of the drive amplitude  $\mathcal{E}_t$  (or, equivalently, the resonator photon number  $\bar{n}_r$ ).

The choice of simulation step size is a trade-off between numerical resolution and physical relevance. While a very small step resolves every avoided crossing, many are too small to be significant. The system's dynamics

### 3 Methodology

are constrained by the resonator's response time, which is set by its linewidth,  $\kappa$ . This physical timescale determines which of the avoided crossings are large enough to actually affect the qubit.

To ensure our simulation captures only these relevant interactions, we link our step size to this timescale. We increment the drive amplitude  $\varepsilon_t$  (related to photon number by  $\bar{n}_r = (\varepsilon_t/2g)^2$ ) using a step of  $\delta\varepsilon_t = \kappa/2\pi$ . This method effectively filters out insignificant crossings, focusing the analysis on the dynamics that cause ionization.

As shown in Figure 3.5(b), we plot the quasienergy spectrum versus the resonator photon number. The plot reveals several avoided crossings (e.g., between  $|1\rangle$  and  $|8\rangle$ ), which are the fingerprints of the multi-photon resonances that drive MISTs. At these points, the system can undergo a transition from a computational state (usually  $|0\rangle$  and  $|1\rangle$ ) to a higher-energy, non-computational ("ionized") state. Figure 3.5(a) shows the abrupt nature of these transitions by plotting the variable  $N_t$ , which represents the transmon population average over a single drive period, as a function of the resonator photon number.

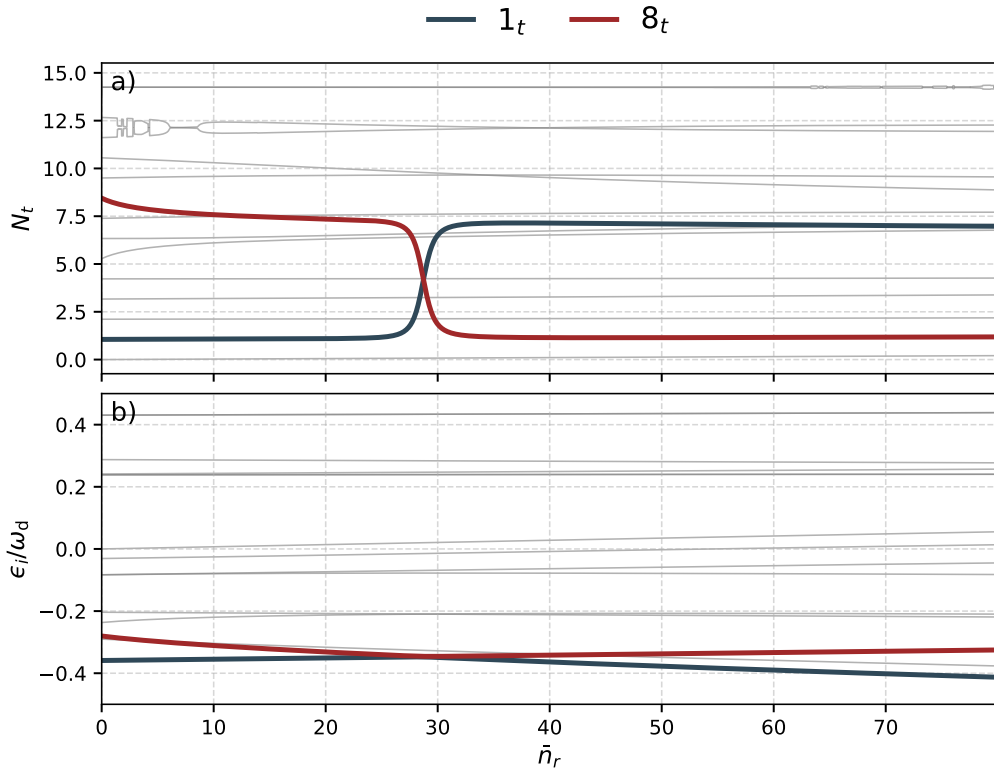


**Figure 3.5** Recreation of Figure 2.3 with our setup data (Table 1) for  $n_g = 0$  (a) Period-averaged transmon population of the Floquet modes and (b) quasienergy spectrum of the Floquet modes as a function of the average resonator photon number  $n_r = (\varepsilon_t/2g)^2$ . The avoided crossings (points where the lines repel each other) indicate the photon numbers where measurement-induced state transitions are likely to occur.

Now we define the critical photon number,  $n_c$ , as the lowest photon number at which a computational state becomes unstable due to such a resonance. As mentioned in Section 2.4, the location of these resonances is highly sensitive to the gate charge  $n_g$ , especially for transitions involving high-energy states. Therefore, to get a realistic prediction, we average the calculated  $n_c$  over a uniform distribution of  $n_g \in [0, 0.5]$ , as shown in Figure 3.6. This range is sufficient because while the transmon Hamiltonian is periodic in  $n_g$  with a period of 1, symmetries at  $n_g = 0$  and  $n_g = 0.5$  cause the system to have an effective periodicity of 0.5 ([Bla+21, Sec. II.D]).

A comparison of our results (Figure 3.6) with the reference work [Dum+24] (Figure 2.4) reveals that the predictions from the semiclassical Floquet model ( $\bar{n}_c$ ) and the Jaynes-Cummings model ( $n_{\text{crit,JC}}$ ) are in closer agreement for our setup data (Table 1). This difference can be attributed to our system's different parameters:

a lower coupling strength  $g$  raises the Jaynes-Cummings threshold  $n_{\text{crit, JC}}$  (see Equation (2.6)), while a smaller resonator linewidth  $\kappa$  tends to lower the Floquet-predicted threshold  $\bar{n}_c$ .

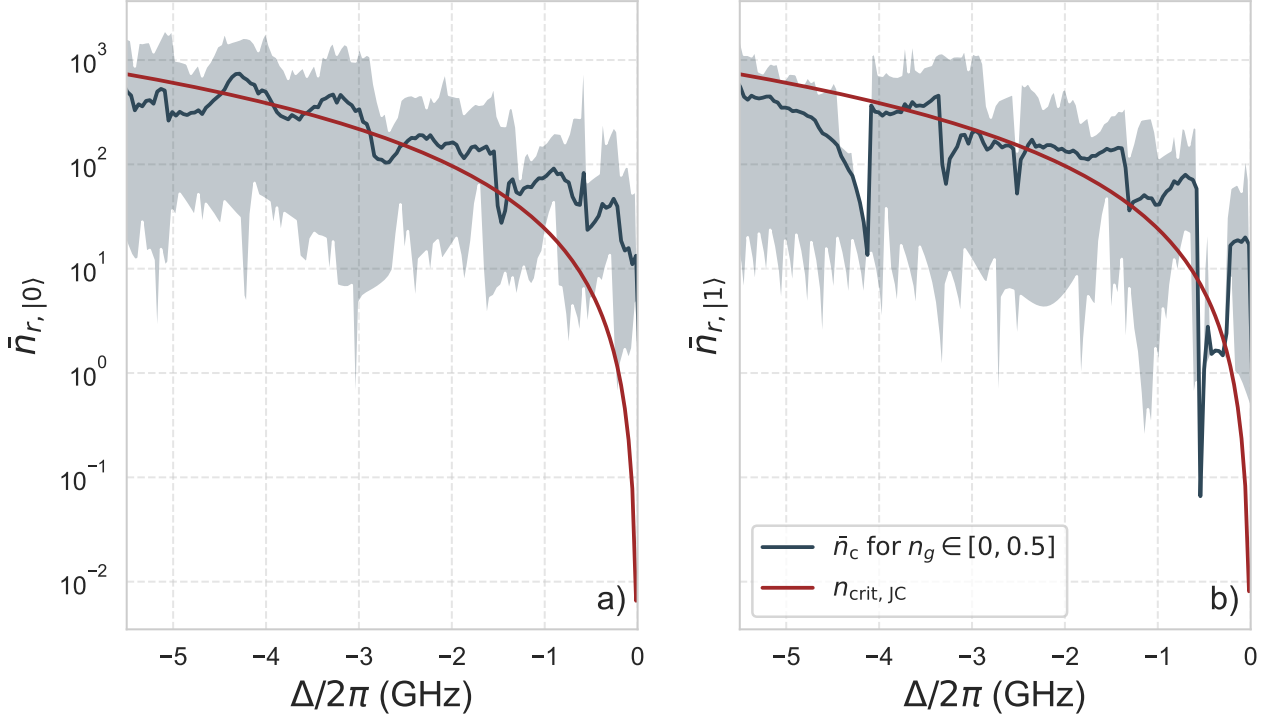


**Figure 3.6** The critical photon number for ionization,  $n_c$ , as a function of qubit-resonator detuning,  $\Delta/2\pi$ . This plot recreates the analysis from Figure 2.4 using our experimental parameters (Table 1) for negative detuning. The solid line shows the critical photon number for the transmon states  $|0\rangle$  (a) and  $|1\rangle$  (b), averaged over 25 values of the gate charge  $n_g \in [0, 0.5]$ . The shaded region represents the spread due to fluctuations of  $n_g$ , highlighting the significant impact of charge noise on MISTS. The red line represents critical photon number  $n_{\text{crit, JC}} = \frac{\Delta^2}{4g^2}$  discussed in Section 2.2.

This framework, therefore, provides an efficient and intuitive method for determining the critical photon number  $\bar{n}_c$ . As we show later, this value gives us a crucial input for our fidelity simulations, setting an upper bound on the readout power to ensure a QND measurement.



## 4 Results and Discussion

It is important to mention that the following analysis is based entirely on numerical simulations. The conclusions drawn in this chapter serve as a starting point for future investigations and must be validated by experimental measurements.

In the previous chapter, we established two different but complementary simulation frameworks. The fidelity simulation (Section 3.1) evaluates readout accuracy as a function of system parameters, including the input power of the readout pulse,  $P_{\text{in}}$ . The semiclassical Floquet analysis (Section 3.2) determines the critical photon number,  $\bar{n}_c$ , at which MISTs become probable, thus setting a physical limit on the resonator's population. We also connected these two frameworks with the crucial link: the relationship between the input power  $P_{\text{in}}$  and the resulting intracavity photon number  $n(t)$ . Now we can conduct a meaningful analysis of how readout fidelity depends on qubit-resonator detuning without violating QND conditions.

### 4.1 Constrained Fidelity Analysis

With the simulation frameworks for readout fidelity and MISTs established, we now perform a combined analysis. The results are synthesized in the comprehensive map shown in Figure 4.1, which plots simulated readout fidelity as a function of both qubit-resonator detuning ( $\Delta/2\pi$ ) and the maximum number of photons in the resonator ( $\bar{n}_r$ ). This photon number is directly related to the input power of the readout pulse, as derived in Section 2.5.

Overlaid on this fidelity map are the critical photon numbers at which MISTs become probable, calculated using the Floquet analysis and averaged over a range of gate charges  $n_g \in [0, 0.5]$ . Similar to Figure 3.6, we plot two key boundaries derived from the Floquet analysis. These boundaries represent the gate-charge averaged critical photon numbers for the ground ( $\bar{n}_{c,|0\rangle}$ ) and excited ( $\bar{n}_{c,|1\rangle}$ ) states. To avoid cluttering the figure, we omitted the shaded region representing the spread over the gate charge  $n_g$ .

These lines effectively partition the parameter space into two functionally distinct regions:

- QND-Safe Region (below the critical photon number lines): In this region, the resonator's photon population is maintained below the MIST threshold, implying that the measurement is expected to be non-demolition. The fidelity values here represent physically achievable and reliable readout outcomes.
- MIST-Prone Region (above the critical photon number lines): Here, the readout power is sufficient to induce unwanted state transitions. While the fidelity simulation might predict high values due to a strong signal, these results are physically unreliable because the initial qubit state is likely corrupted during the measurement.

Our primary objective is to identify the detuning  $\Delta$  that maximizes the achievable readout fidelity within the QND-safe operating regime.

### 4.1.1 Interpretation of Results

Figure 4.1 reveals a clear trade-off between MIST avoidance and signal quality, leading to three distinct operational regimes:

#### **Small Detuning Regime ( $|\Delta/2\pi| < 1.5 \text{ GHz}$ )**

This regime is doubly problematic. First, the extremely large dispersive shift  $\chi$  pushes the state-dependent resonator frequencies far from the readout pulse frequency, resulting in inefficient driving and a weak signal. This problem was discussed in Section 3.1.3. Second, the critical photon number ( $\bar{n}_c$ ) is exceptionally low. The combination of a poor signal response and the strict power limitations required for QND operation makes this regime suboptimal for achieving high-fidelity readout.

#### **Large Detuning Regime ( $|\Delta/2\pi| > 4.5 \text{ GHz}$ )**

Conversely, at large detunings, the MIST threshold is very high, removing it as a primary constraint. However, the small dispersive shift ( $\chi \propto 1/\Delta$ ) makes the qubit states nearly indistinguishable. This leads to a poor SNR and fundamentally low fidelity, regardless of the available readout power.

#### **Optimal Operating Window ( $|\Delta/2\pi| \approx 3.5 - 4 \text{ GHz}$ )**

This range represents an optimal trade-off window: the MIST threshold here is high enough to permit a strong readout pulse, while the dispersive shift is large enough for a good state distinguishability and efficient driving. This alignment allows for high fidelity to be achieved safely within the QND regime, making it the most promising parameter space for device design. However, it is important to note that this specific range is not a general solution, as the performed simulations are highly dependent on the device parameters used in this work (Table 1).

Finally, the map suggests that increasing detuning indefinitely is not an optimal strategy. The iso-fidelity contours rise more steeply with  $\Delta$  than the  $\bar{n}_c$  boundaries. This indicates that at very large detunings, the power required to reach a high fidelity will eventually exceed the MIST threshold. Our analysis thus confirms the existence of an optimal, finite detuning for maximizing QND readout fidelity.

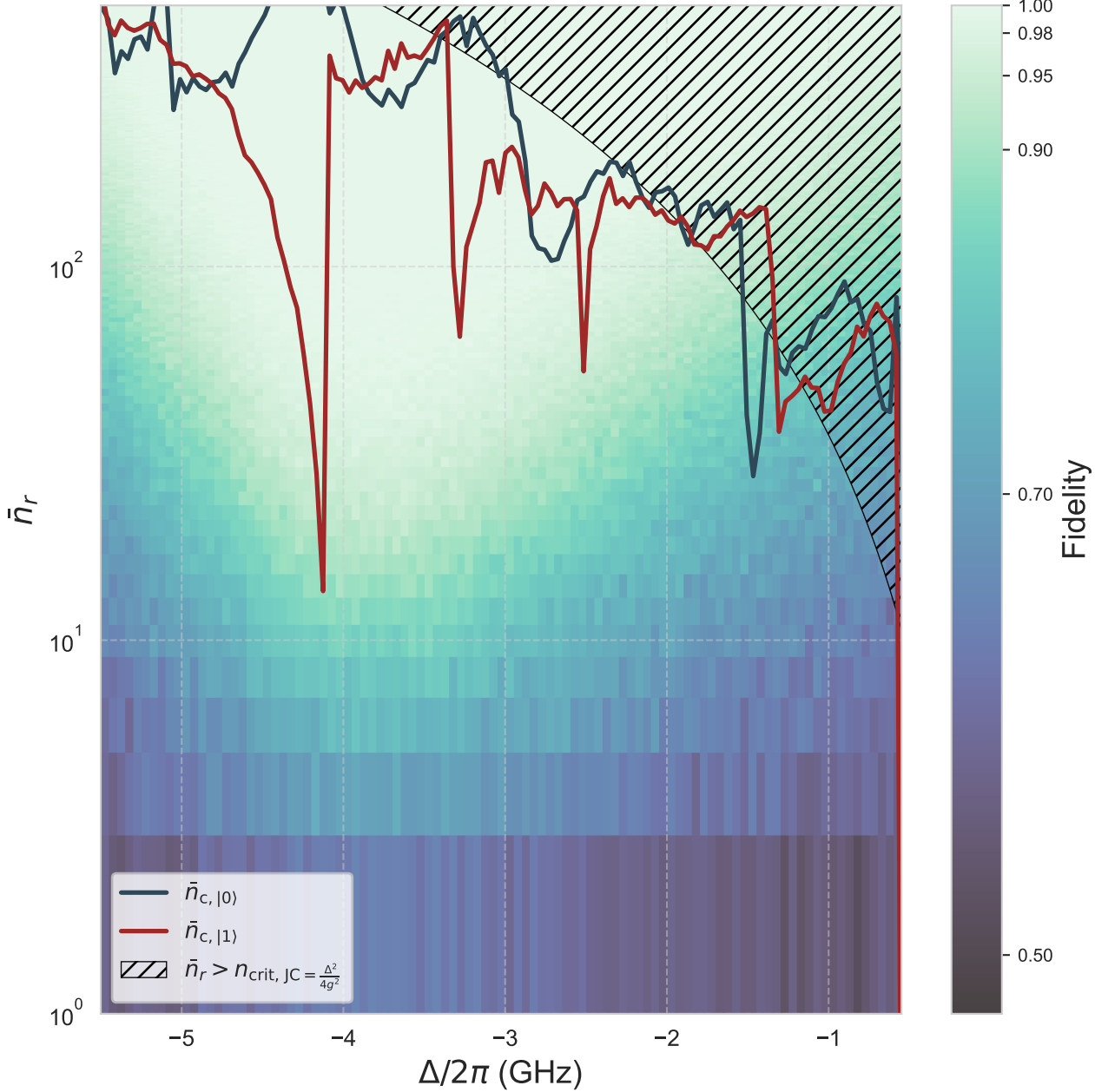


**Figure 4.1** Combined analysis of readout fidelity and MISTs. The 2D colormap shows the simulated readout fidelity as a function of qubit-resonator detuning ( $\Delta/2\pi$ ) and the maximum resonator photon number ( $n_r$ ) built up during the  $2\mu\text{s}$  square readout pulse with the carrier frequency  $\omega_d = (\omega_{r,|0\rangle} + \omega_{r,|1\rangle})/2$ . The red and dark blue lines indicate the averaged critical photon numbers, which serve as the upper boundary for more probable QND measurements. Varying the detuning effectively sweeps through different multi-photon resonances, which appear as the distinct sharp dips in the plot. The shaded area represents incorrect fidelity predictions because of the invalid assumption of  $n_{\text{crit},\text{JC}} \gg n_r$  used in the derivation of Equation (2.8).



## 5 Conclusion and Outlook

This thesis addressed the critical trade-off between speed and fidelity in superconducting qubit readout, which is fundamentally limited by MISTs. By investigating different qubit-resonator detuning regimes,  $\Delta$ , we aimed to suppress these unwanted transitions.

We developed a predictive model by integrating a readout fidelity simulation with a semiclassical Floquet analysis. This combined framework allowed us to perform a constrained analysis, evaluating the achievable readout fidelity under the physical requirement of avoiding MISTs. Our central finding is the identification of an optimal detuning window,  $\Delta/2\pi \approx [-4, -3.5]$  GHz. This window successfully balances the conflicting demands of large detuning (to raise the MIST photon threshold) and small detuning (to ensure a strong, distinguishable signal via a large dispersive shift,  $\chi$ ).

While this work provides a robust, data-driven framework for designing readout systems for the large-detuning regime, its conclusions are based on numerical modeling. A crucial next step is the experimental verification of these predictions. To confirm the predicted balance between high fidelity and MIST suppression, future work should involve fabricating and measuring devices with tunable qubit-resonator detuning ( $\Delta$ ), achievable through frequency-adjustable qubits or resonators. Such experiments would not only validate the simulation framework but also contribute to the development of faster and more reliable quantum processors.

The simulation frameworks presented here can be readily extended. In our analysis, we focused on simple rectangular readout pulses for simplicity. However, the pulse shape is a critical degree of freedom for controlling quantum dynamics. It is important to note that the Floquet analysis is independent of the pulse shape as long as its envelope varies slowly compared to the carrier frequency. Furthermore, our fidelity simulation can readily accept arbitrary pulse shapes as input. A natural next step would be to explore advanced pulse shapes, such as those with smooth rise/fall times (e.g., Gaussian, DRACHMA [Jer+24]). Such pulses could be designed to traverse avoided crossings diabatically, potentially allowing for higher readout power even at smaller detunings.



# Appendix

## A Additional Figures

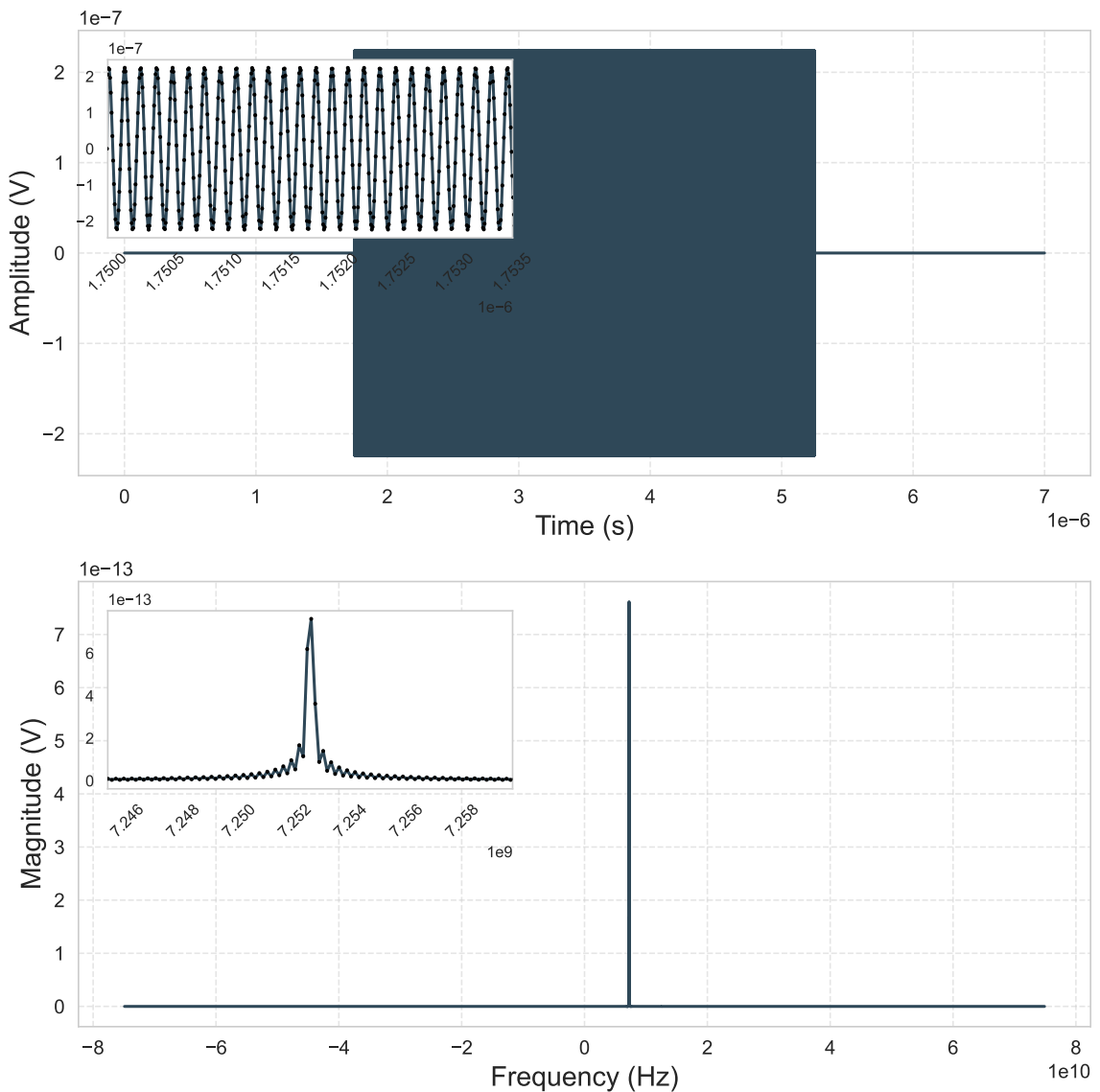


**Figure 1** Rectangular pulse with duration  $t = 3.5 \mu\text{s}$ , carrier frequency  $f = 7.252534 \text{ GHz}$ , and attenuated power  $P_{\text{attenuated}} = -123 \text{ dBm}$ , shown in time and frequency domains with zoom-ins illustrating discretization resolution. The total signal duration was extended to  $t_{\text{total}} = 7 \mu\text{s}$  for improved frequency-domain resolution after FFT.

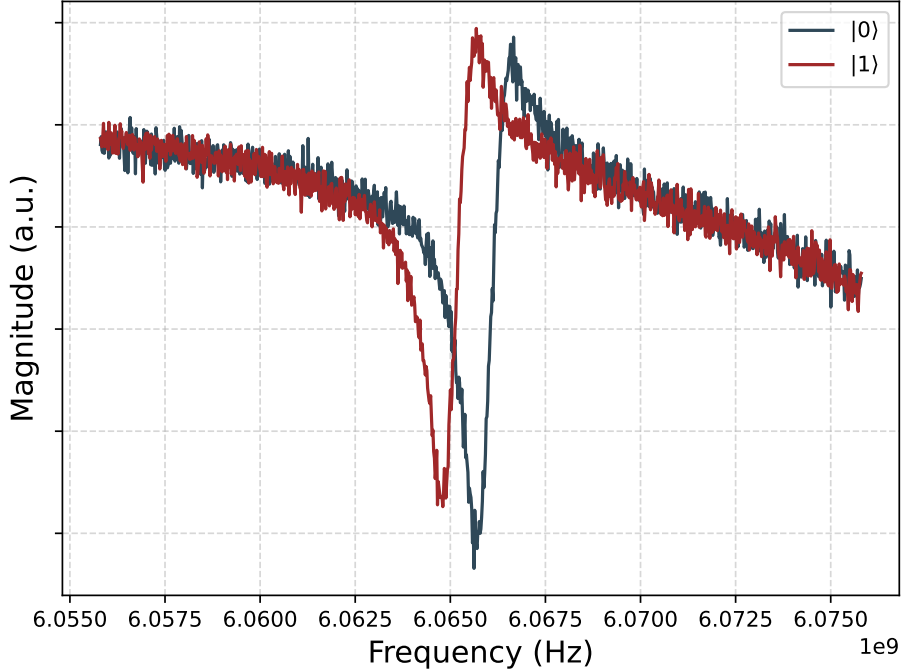


**Figure 2** Experimentally obtained  $S_{21}$  spectra of the resonator coupled to the qubit in state  $|0\rangle$  (blue) and in state  $|1\rangle$  (red).

## B Tables

**Table 1** Device parameters.

Device Parameters	
<i>Measured Parameters</i>	
0-1 transition frequency $\omega_{01}/2\pi$ (GHz)	3.845965
1-2 transition frequency $\omega_{12}/2\pi$ (GHz)	3.602265
Resonator frequency at $ 0\rangle$ , $\omega_{r, 0\rangle}/2\pi$ (GHz)	6.065853
Resonator frequency at $ 1\rangle$ , $\omega_{r, 1\rangle}/2\pi$ (GHz)	6.064932
Resonator frequency at $ 2\rangle$ , $\omega_{r, 2\rangle}/2\pi$ (GHz)	6.064094
<i>Derived and Fitted Parameters</i>	
First anharmonicity $\alpha_1/2\pi = f_{12} - f_{01}$ (MHz)	-243.700
Dispersive shift $\chi/2\pi = (\omega_{r, 1\rangle} - \omega_{r, 0\rangle})/4\pi$ (kHz)	-460.570
Bare resonator frequency $f_r$ (GHz) <sup>a</sup>	6.0650
Resonator linewidth $\kappa/2\pi$ (kHz) <sup>a</sup>	550
Josephson energy $E_J/h$ (GHz) <sup>a</sup>	9.8266
Charging energy $E_C/h$ (GHz) <sup>a</sup>	0.2106
$E_J/E_C$ <sup>a</sup>	46.651
Transmon-resonator coupling strength $g/2\pi$ (MHz) <sup>a</sup>	101.7

<sup>a</sup> Parameters obtained from fitting.

# List of Figures

2.1	Potential energy landscape and energy levels of a quantum harmonic oscillator (QHO) compared to a transmon qubit. The QHO (a) has equally spaced energy levels (b), while the transmon's (c) anharmonic potential (d) leads to non-equidistant levels, enabling selective control of qubit states. Figure taken from [Kra+19]. . . . .	4
2.2	Heterodyne detection schematic. (a) The signal $s(t)$ at frequency $\omega_{RF}$ is mixed with a local oscillator at $\omega_{LO}$ , producing two quadratures at intermediate frequency $\omega_{IF}$ , $90^\circ$ out of phase. (b) Two ADC channels digitize these after a readout delay $\tau_{rd}$ and sampling time $\tau_s$ (white dots show samples). (c) Post-processing yields a single point in the $(I, Q)$ -plane per shot. Repeating this many times forms a 2D histogram with a Gaussian distribution due to noise. Figure taken from [Kra+19]. . . . .	6
2.3	Branch analysis for a transmon-resonator system at negative detuning ( $\omega_q < \omega_r$ ). (a) The average transmon population $N_t$ for each branch shows an abrupt "swapping" of character between branches (e.g., between $B_{1,t}$ and $B_{7,t}$ ) at specific resonator photon numbers $N_r$ . (b) This swapping corresponds to avoided crossings in the energy spectrum of the system, shown here folded modulo $\omega_r$ . The dotted lines mark the photon numbers where these strong interactions occur. (c) Dynamics of the driven transmon-resonator system when initializing in the excited state $ 1_t, 0_r\rangle$ . Figure taken from [Dum+24]. . . . .	10
2.4	Critical photon number for ionization as a function of detuning, adapted from [Dum+24]. The plots show the threshold for the (a, b) ground and (c, d) excited states. The colored background represents the final transmon population from time-dynamics simulations. The overlaid lines show the critical photon number that the full quantum model (pink) and the semiclassical Floquet model (red) predicted. The agreement between the two models is excellent. . . . .	11
2.5	Simulated intracavity ( $\kappa/2\pi = 0.55$ MHz) photon number based on Equation (2.26) during a square readout pulse of length $t$ with a fixed input power $P_{in} = -123$ dBm (a) Photon number built up over time, $n_r(t)$ . The resonator populates on a timescale determined by its decay rate $\kappa$ . (b) The maximum photon number reached at the end of the pulse, $n_{r,max} = n_r(t_{pulse} = 2\mu s)$ , as a function of the qubit-resonator detuning $\Delta/2\pi$ . For a fixed input power and drive frequency, the efficiency of populating the resonator is highly dependent on the detuning from the pulled resonance frequency, leading to a strong dependence of $n_{r,max}$ on $\Delta$ . (c) Built up photon number in dependence of time $t$ and detuning $\Delta/2\pi$ . . . . .	12
3.1	(a) The qubit system and the readout path with all three amplification stages, which contributed to the considered noise. (b) Simulation methodology for superconducting qubit readout fidelity, combining resonator modeling with noise and signal simulation. Adapted from [Won+23]. . . . .	14
3.2	(a) Chip design for S-parameter simulation of the $ 0\rangle$ state. The red rectangle highlights the region shown in (b). (b) A close-up of the finite element mesh used during the simulation, illustrating the mesh density. . . . .	15
3.3	Simulations for reading $ 0\rangle$ and $ 1\rangle$ states with the following parameters: $f_r = 7.252534$ GHz, $\frac{\chi}{2\pi} = 156$ kHz, $Q \approx 48 \cdot 10^3$ , $t_{rect. pulse} = 3.5 \mu s$ , $P_{attenuated} = -123$ dBm (see Appendix A) (a) Comparison between measurement and simulation of the system fidelity. Adapted from [Won+23]. (b) Our simulation of the system readout fidelity. . . . .	16

3.4	Readout fidelity in dependence on $\Delta$ . (a) Readout fidelity versus qubit-resonator detuning ( $\Delta/2\pi$ ), with the corresponding dispersive shift ( $\chi/2\pi$ ) shown on the top x-axis. The fidelity exhibits a clear peak at an optimal detuning. (b) Representative $S_{21}$ spectra for qubit states $ 0\rangle$ (blue) and $ 1\rangle$ (red), illustrating the resonator's magnitude response at two different detunings: $\Delta/2\pi = -0.5$ GHz (small detuning, large $\chi$ ) and $\Delta/2\pi = -5.5$ GHz (large detuning, small $\chi$ ). The black curve indicates the fixed spectrum of the scaled rectangular readout pulse. These plots collectively explain the non-monotonic fidelity behaviour, demonstrating the critical trade-off between state distinguishability (separation of blue and red curves, proportional to $\chi$ ) and signal strength (overlap of these curves with the readout pulse). Maximum fidelity is achieved at intermediate detunings where both distinguishability and signal strength are optimized.	17
3.5	Recreation of Figure 2.3 with our setup data (Table 1) for $n_g = 0$ (a) Period-averaged transmon population of the Floquet modes and (b) quasienergy spectrum of the Floquet modes as a function of the average resonator photon number $n_r = (\varepsilon_t/2g)^2$ . The avoided crossings (points where the lines repel each other) indicate the photon numbers where measurement-induced state transitions are likely to occur.	18
3.6	The critical photon number for ionization, $n_c$ , as a function of qubit-resonator detuning, $\Delta/2\pi$ . This plot recreates the analysis from Figure 2.4 using our experimental parameters (Table 1) for negative detuning. The solid line shows the critical photon number for the transmon states $ 0\rangle$ (a) and $ 1\rangle$ (b), averaged over 25 values of the gate charge $n_g \in [0, 0.5]$ . The shaded region represents the spread due to fluctuations of $n_g$ , highlighting the significant impact of charge noise on MISTs. The red line represents critical photon number $n_{\text{crit,JC}} = \frac{\Delta^2}{4g^2}$ discussed in Section 2.2.	19
4.1	Combined analysis of readout fidelity and MISTs. The 2D colormap shows the simulated readout fidelity as a function of qubit-resonator detuning ( $\Delta/2\pi$ ) and the maximum resonator photon number ( $n_r$ ) built up during the 2 $\mu$ s square readout pulse with the carrier frequency $\omega_d = (\omega_{r, 0\rangle} + \omega_{r, 1\rangle})/2$ . The red and dark blue lines indicate the averaged critical photon numbers, which serve as the upper boundary for more probable QND measurements. Varying the detuning effectively sweeps through different multi-photon resonances, which appear as the distinct sharp dips in the plot. The shaded area represents incorrect fidelity predictions because of the invalid assumption of $n_{\text{crit,JC}} \gg n_r$ used in the derivation of Equation (2.8).	23
1	Rectangular pulse with duration $t = 3.5$ $\mu$ s, carrier frequency $f = 7.252534$ GHz, and attenuated power $P_{\text{attenuated}} = -123$ dBm, shown in time and frequency domains with zoom-ins illustrating discretization resolution. The total signal duration was extended to $t_{\text{total}} = 7$ $\mu$ s for improved frequency-domain resolution after FFT.	27
2	Experimentally obtained $S_{21}$ spectra of the resonator coupled to the qubit in state $ 0\rangle$ (blue) and in state $ 1\rangle$ (red).	28

# Bibliography

- [Ans24] Ansys, Inc. *Ansys HFSS*. Version 2024 R1. Canonsburg, PA, 2024.
- [Bla+04] A. Blais et al. “Cavity quantum electrodynamics for superconducting electrical circuits: An architecture for quantum computation”. In: *Phys. Rev. A* 69 (6 June 2004), p. 062320.
- [Bla+21] A. Blais et al. “Circuit Quantum Electrodynamics”. In: *Reviews of Modern Physics* 93.2 (2021), p. 025005.
- [Cle+10] A. A. Clerk et al. “Introduction to quantum noise, measurement, and amplification”. In: *Rev. Mod. Phys.* 82 (2 Apr. 2010), pp. 1155–1208.
- [Dum+24] M. F. Dumas et al. “Measurement-Induced Transmon Ionization”. In: *Physical Review X* 14.4 (Oct. 2024). ISSN: 2160-3308.
- [Jer+24] M. Jerger et al. *Dispersive Qubit Readout with Intrinsic Resonator Reset*. 2024. arXiv: 2406.04891 [quant-ph].
- [Kha+12] M. S. Khalil et al. “An analysis method for asymmetric resonator transmission applied to superconducting devices”. In: *Journal of Applied Physics* 111.5 (Mar. 2012). ISSN: 1089-7550.
- [Kra+19] P. Krantz et al. “A Quantum Engineer’s Guide to Superconducting Qubits”. In: *Applied Physics Reviews* 6.2 (2019), p. 021318.
- [Won+23] H. Y. Wong et al. “A simulation methodology for superconducting qubit readout fidelity”. In: *Solid-State Electronics* 201 (Mar. 2023), p. 108582. ISSN: 0038-1101.